J. Fluid Mech. (2021), *vol*. 916, A9, doi:10.1017/jfm.2021.168

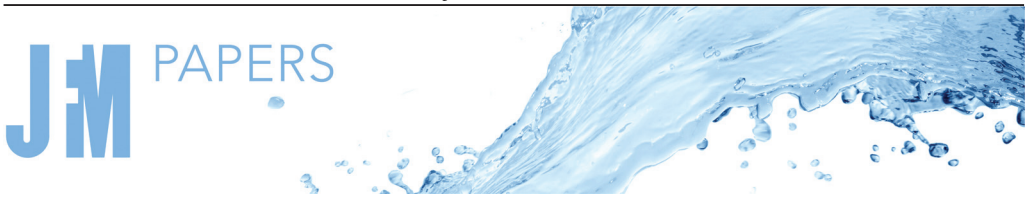

Universality of small-scale motions within the turbulent/non-turbulent interface layer

Marco Zecchetto[1] **and Carlos B. da Silva**[1],†

[1]LAETA, IDMEC, Instituto Superior Técnico, Universidade de Lisboa, Lisboa, Portugal

(Received 23 June 2020; revised 22 December 2020; accepted 17 February 2021)

The universality of the statistics of small-scale motions within the turbulent/non-turbulent interface (TNTI) layer that exists at the edges of turbulent free shear flows (i.e. mixing layers) and in turbulent boundary layers is analysed using direct numerical simulations of turbulent jets, wakes and in turbulent fronts evolving without mean shear. The Taylor based Reynolds number of the simulations is $Re_\lambda \gtrsim 200$ while the resolution is comparable to the Kolmogorov micro-scale $\Delta x \approx \eta$. It is shown that, when properly normalised by using the local Kolmogorov velocity and length scales, the statistics of the vorticity, strain and related quantities, such as the invariants of the velocity gradient tensor, are universal, i.e. virtually equal for the same position within the TNTI layer, which implies the universality of the small-scale 'nibbling' associated with the turbulent entrainment mechanism. The results show that the small scales of motion near the TNTI layer are statistically very close to homogeneous, except for a distance of about 10 Kolmogorov micro-scales from the outer surface of the TNTI layer. The proposed normalisation allows for a much more clear identification of the viscous superlayer and the turbulent sublayer within the TNTI layer.

Key words: shear layer turbulence, turbulence simulation

1. Introduction

The turbulent/non-turbulent interface (TNTI) layer is the sharp and highly contorted interface that exists in jets, wakes, mixing layers and boundary layers, separating the flow field into two distinct regions: a turbulent (T) region and a region of irrotational (IR) or non-turbulent (NT) flow (da Silva *et al.* 2014). The flow dynamics within the TNTI layer determines the turbulent entrainment (TE) mechanism, which is the process by which fluid in the IR flow region is continually drawn into the T region, increasing its extent as measured by the shear layer or boundary layer thickness. Turbulent entrainment is crucial to many processes in engineering and the environment, such as the transport of passive and active scalars, e.g. heat (da Silva *et al.* 2014), which motivates the investigation of the

† Email address for correspondence: carlos.silva@ist.utl.pt

© The Author(s), 2021. Published by Cambridge University Press

https://doi.org/10.1017/jfm.2021.168 Published online by Cambridge University Press

TNTI layer. The study of the flow dynamics near the TNTI layer starts with the seminal work of Corrsin & Kistler (1955) who suggested that (i) the key quantity to analyse the TE mechanism is the vorticity $\omega_i = \epsilon_{ijk}\partial u_j/\partial x_k$ (or the enstrophy $\omega^2 = \omega_i\omega_i$), where u_i is the velocity vector field, since the NT and T regions can be rigorously defined as flow regions with $\omega_i = 0$ and $\omega_i \neq 0$, respectively. Turbulent entrainment can then be understood as the mechanism causing the increase of vorticity (or enstrophy) across a separating layer between the NT and T regions. Corrsin & Kistler (1955) also hypothesised that (ii) there must be a strong vorticity increase (jump) caused by viscous diffusion in this separating layer, which they named the viscous superlayer. Finally, (iii) they estimated that the thickness of the VSL (δ_ν) should be equal to the Kolmogorov micro-scale (η), i.e. $\delta_\nu \approx \eta$, where $\eta = (\nu^3/\varepsilon)^{1/4}$, $\varepsilon = 2\nu S_{ij}S_{ij}$ is the viscous dissipation rate inside the turbulent region, ν is the kinematic viscosity of the fluid and $S_{ij} = (\partial u_i/\partial x_j + \partial u_j/\partial x_i)/2$ is the rate of strain tensor.

Recently, the analysis of the TNTI layer became more accessible due to the development of new metrics such as the conditional statistics in relation to the TNTI position (Bisset, Hunt & Rogers 2002; da Silva & Pereira 2008; Westerweel *et al.* 2009; Watanabe *et al.* 2014). It turns out that the TNTI has a two layer structure, comprising a viscous superlayer (VSL) where the effects of vorticity diffusion dominate, and a turbulent sublayer (TSL) where the enstrophy production dominates (Taveira *et al.* 2013; van Reeuwijk & Holzner 2014; Taveira & da Silva 2014), and that the strong vorticity jump bridging the IR and T regions, previously hypothesised by Corrsin & Kistler (1955), actually fills the entire TNTI layer, and not only the viscous dominated (VSL) region.

The VSL was directly observed and measured only recently, by using very fine direct numerical simulation (DNS) (Taveira & da Silva 2014). It consists of a continuous layer forming the outer layer of the TNTI (as seen from inside the T region), with a mean thickness of $\langle\delta_\nu\rangle \approx 4$–$5\eta$, which is explained by the role of the intense vortices from the T region in defining the shape of the TNTI layer. Indeed, the shape of the TNTI layer is actually imposed by the 'last row' of eddies from the T region that are closest to the IR region. The correct scaling of the VSL had been anticipated not only by Corrsin & Kistler (1955), but more recently by Holzner & Luthi (2011) using dimensional analysis considerations.

On the other hand, the TSL has a slightly larger width, with a mean thickness that was recently shown to be $\langle\delta_\sigma\rangle \approx 10\eta$ (Silva, Zecchetto & da Silva 2018), which is again related to the intense vortices in the vicinity of the TNTI layer (da Silva, dos Reis & Pereira 2011; Watanabe *et al.* 2016*b*; Watanabe, da Silva & Nagata 2019), so that the total mean extent of the TNTI layer is $\langle\delta_\omega\rangle \approx \langle\delta_\nu\rangle + \langle\delta_\sigma\rangle \approx 15\eta$. Thus, both sublayers within the TNTI layer scale with the Kolmogorov micro-scale.

One of the most interesting observations described in many recents works consists in the shape of the enstrophy (or vorticity magnitude) and of the enstrophy equation terms, as a function of the distance from the TNTI layer position, using a procedure pioneered by Bisset *et al.* (2002) and perfected in several subsequent works (Westerweel *et al.* 2005; da Silva & Pereira 2008; Westerweel *et al.* 2009). This is typically observed by collecting statistics at fixed distances within the TNTI layer (conditional profiles) and has been used extensively to analyse the TNTI layer in many experimental and numerical works.

Experimental works include the results from Westerweel *et al.* (2002, 2009) who analysed the out-of-plane vorticity component of a round submerged liquid jet, Chauhan *et al.* (2014*b*) who studied the spanwise vorticity of a zero-pressure-gradient turbulent boundary layer and Holzner *et al.* (2007) who investigated twice the enstrophy ($\omega_i\omega_i$) in a turbulent flow without mean shear.

https://doi.org/10.1017/jfm.2021.168 Published online by Cambridge University Press

Numerical works include Holzner *et al.* (2007) who studied conditional profiles of $\omega_i\omega_i$ from a temporal simulation of a turbulent front evolving without mean shear, Taveira & da Silva (2013) who showed conditional profiles of all the absolute values of the vorticity vector components, Attili, Cristancho & Bisetti (2014) who assessed the vorticity magnitude in an incompressible spatially developing mixing layers and Watanabe *et al.* (2014) who investigated the profiles of both the enstrophy ($\omega_i\omega_i/2$) and vorticity magnitude in a spatially developing planar jet with chemical reactions.

The conditional profile of vorticity magnitude has been computed in temporally developing plane wakes (Bisset *et al.* 2002), plane jets (da Silva *et al.* 2011), compressible reacting mixing layers (Jahanbakhshi & Madnia 2018), compressible mixing layers (Vaghefi & Madnia 2015; Jahanbakhshi & Madnia 2016), stably stratified mixing layers (Watanabe *et al.* 2016*a*), boundary layers (Ishihara, Ogasawara & Hunt 2015; Borrell & Jiménez 2016; Watanabe, Zhang & Nagata 2018), planar jets, shear-free turbulence and mixing layers (Watanabe *et al.* 2019). Other examples of the conditional statistic of vorticity (or related quantities) can be found as well in Silva *et al.* (2018), Breda & Buxton (2019), Cimarelli *et al.* (2015).

All these works report a sharp jump in the vorticity (or enstrophy) across the TNTI layer, but the way this jump is normalised, as well of its precise shape, present some discrepancies. A comparison between the profiles of vorticity magnitude (or enstrophy) across the TNTI layer obtained in several different flows is described in da Silva *et al.* (2014), at a time where the mean thickness of this jump (at sufficiently high Reynolds numbers) had not yet been established, which occurred only recently (Silva *et al.* 2018). However, it is clear that the shape of these profiles is different.

Similarly, many authors have described the conditional enstrophy budgets near the TNTI layer, e.g. Holzner *et al.* (2007), da Silva & Pereira (2008), Watanabe *et al.* (2014), Silva *et al.* (2018). Typically, the enstrophy production and dissipation are balanced in the turbulent core region of the flow, whereas within the TNTI layer, the enstrophy diffusion dominates the VSL and is overtaken by the enstrophy production in the TSL. Even though all the published results of these quantities display a relatively similar qualitative shape, the details of each profile are not equal, and exhibit clear differences when computed from different flows and different Reynolds numbers.

However, since the vorticity (or the enstrophy) is associated with the smallest scales of motion, and given that in fully developed turbulence the small scales tend to be universal, one would expect the vorticity (or the enstrophy) to exhibit some sort of universality. Indeed, our present understanding of the TE is that the entrainment rate is imposed by the large scales of motion, while the smallest scales adjust to that rate and direct it through the 'nibbling' mechanism (Westerweel *et al.* 2005). In analogy with the energy cascade mechanism, if the large-scale motions shape the TNTI such that the global entrainment is independent of viscosity then the statistics of the small scales of motion responsible for the entrainment should be universal, i.e. equal in TNTIs from different flows. For instance, when properly normalised the mean profiles of these quantities across the TNTI layer, and of other small-scale quantities, should be equal in jets, wakes and mixing layers.

Some results are consistent with this possibility. Watanabe *et al.* (2019) showed that the non-dimensional dissipation rate $C_\epsilon = \varepsilon L/u'^3$, where L and u' are the integral length scale of turbulence and the streamwise velocity fluctuation, respectively, has three distinct power laws $C_\varepsilon \sim Re_\lambda^\alpha$, inside the VSL, TSL and T (core) regions (Re_λ is the turbulent Reynolds number and α is the power law value), which are exactly the same (i.e. same α for the same layer) for planar jets, mixing layers and free shear turbulence, where L, ε and u'^3 are locally computed inside each one of the sublayers.

https://doi.org/10.1017/jfm.2021.168 Published online by Cambridge University Press

In the present paper we use DNS of three different flow types: planar jets, planar wakes and shear-free turbulence (a turbulent front evolving without mean shear) to show that, when properly normalised, all the small-scale statistics of the flow within the TNTI layer collapse into the same curves/profiles. We focus the analysis into two small-scale variables: the enstrophy (or vorticity magnitude) and strain, and related variables. The normalisation consists of simply using the mean local Kolmogorov velocity and time scales of the flow, computed at each location within the TNTI layer. The picture that emerges from all these results is that indeed the statistics of the small-scale variables within the TNTI layer are universal, i.e. equal in very different flows, and at different Reynolds numbers (provided the Reynolds number is sufficiently high) and support the concept that the 'nibbling' eddy motions acting on the TNTI layer are indeed universal, i.e. equal in all flows. It is important to clarify that in no way do we intend to claim any sort of universality for the large scales of motion associated with the entrainment dynamics, e.g. it is well known that the (large-scale) entrainment characteristics are very different between planar and round jets.

This paper is organised as follows. The next section (§ 2) describes the DNS used in the present work, together with the procedure used to obtain statistics in relation to the TNTI layer position. Section 3 describes the universality of the small-scale flow variables within the TNTI layer, as perceived from analysing several statistics of the enstrophy, strain and the invariants of the velocity gradient tensor. The paper ends with § 4 with an overview of the main results of the paper.

2. Direct numerical simulations

This section describes the Navier–Stokes solver and the physical and computational parameters employed in all the simulations used in the present work. The new DNS of wakes are validated against the existing experimental and numerical data and the procedure to obtain conditional statistics, in relation to the distance from the TNTI position, is reviewed.

2.1. *Numerical methods and computational parameters*

Direct numerical simulations of shear-free turbulence (SFT), turbulent planar jets (JET) and turbulent planar wakes (WAKE) were carried out using an in-house code to solve the Navier–Stokes equations. The solver uses classical pseudo-spectral methods (collocation method) for spatial discretization (Canuto *et al.* 1987), and a three-step third-order explicit Runge–Kutta scheme for the temporal advancement (Williamson 1980). The simulations are fully de-aliased using the 2/3 rule and use an uniform and isotropic grid ($\Delta x = \Delta y = \Delta z$). This code has already been used by the authors and is described in detail in Silva *et al.* (2018) and the references therein. The simulations essentially differ in the details of the initial velocity fields and the main physical and computational parameters are summarized in table 1.

One SFT (SFT_{202}) simulation was carried out in a periodic box of size $2\pi \times 2\pi \times 2\pi$ with 1536^3 collocation points using a procedure similar to Perot & Moin (1995), da Silva & Taveira (2010), Taveira & da Silva (2014), Cimarelli *et al.* (2015). The initial turbulent field is issued from a previously run DNS of forced homogeneous isotropic turbulence (HIT), using the forcing scheme proposed by Alvelius (1999), with a peak forcing concentrated at the three wavenumbers centred at $k_p = 2$, and an initial Taylor-based Reynolds number equal to $Re_\lambda = 405$, for a resolution of $k_{max}\eta = 1.48$. The initial turbulence integral scale

https://doi.org/10.1017/jfm.2021.168 Published online by Cambridge University Press

	Re_H	$\langle Re_\lambda \rangle_T$	$N_x \times N_y \times N_z$	$L_x \times L_y \times L_z$	Δ_x/η
SFT_{202}	—	202	$1536 \times 1536 \times 1536$	$2\pi \times 2\pi \times 2\pi$	1.1
JET_{193}	8000	193	$1536 \times 1536 \times 768$	$7H \times 7H \times 3.5H$	1.0
JET_{276}	12 000	276	$2048 \times 2048 \times 1024$	$7H \times 7H \times 3.5H$	1.1
$WAKE_{259}$	16 000	259	$2048 \times 2048 \times 512$	$7H \times 7H \times 1.75H$	1.3
$WAKE_{266}$	16 000	266	$2048 \times 2048 \times 512$	$7H \times 7H \times 1.75H$	1.4
$WAKE_{305}$	18 000	305	$2048 \times 2048 \times 512$	$7H \times 7H \times 1.75H$	1.3

Table 1. Summary of the temporal simulations of shear free turbulence (SFT), planar jets (JET) and planar wakes (WAKE). The data given in the table refer to the field/time instant used in the subsequent analysis. Here $(N_x \times N_y \times N_z)$ is the number of collocation points used in the streamwise (x), normal (y) and spanwise (z) directions, respectively; $(L_x \times L_y \times L_z)$ is the size of the computational domain in the same directions; Re_H is the initial Reynolds number for the temporal jet and wake simulations; $\langle Re_\lambda \rangle_T$ is the Reynolds number based in the Taylor micro-scale in the turbulent core region of the flow computed from conditional statistics (means) taken from an instantaneous field at the self-similar regime (see text for details); Δ_x/η is the resolution normalised by the Kolmogorov micro-scale, where η is taken from the centreline of the flow (at the middle plane of the turbulent core region).

is equal to $L = 1.2$, which is roughly 5.2 times smaller than the computational domain size. The SFT_{202} simulation starts with an initial transient (intermediate) simulation, where the velocity fields obtained from HIT are convoluted by a profile that essentially maintains the velocity $u_i(\boldsymbol{x}, t)$, of the HIT simulation in $-\pi/4 \leq y \leq +\pi/4$, while artificially setting to $u_i(\boldsymbol{x}, t) = 0$ the velocity field in the region $|y| \geq \pi/4$ (Silva *et al.* 2018). As in Cimarelli *et al.* (2015), the convolution profile used here is similar to the hyperbolic tangent profile used in the JET simulations (see below) so that the transition region between the velocity field from HIT and the region with $u_i(\boldsymbol{x}, t) = 0$ is smooth. As in Perot & Moin (1995), during this intermediate simulation, the time step is kept constant and very small, with roughly $1/10$ of that used in the HIT simulations. The true SFT_{202} simulation is then started from this initial condition, whereby the initial isotropic turbulence flow region spreads into the IR (quiescent) region, in the absence of mean shear. Therefore, two distinct (upper and lower) TNTI layers develop within the computational domain, as the turbulence slowly decays within the core of the turbulent region. The present analysis uses only a single (one) instantaneous field from this simulation when the mean conditional Reynolds number in the turbulent core region is equal to $\langle Re_\lambda \rangle_T = 202$ (see the next section for the details on the computation of this Reynolds number), while the resolution is $\Delta x/\eta = 1.13$. At this instantaneous time instant the mean position of the two (upper and lower) TNTIs is $|y_I| \approx \pi/2$, by which time no influence of the periodicity can be observed in the statistics far from the TNTI layer. This SFT_{202} simulation has been previously used in Silva *et al.* (2018).

For the temporal planar jet (JET) and planar wake (WAKE) simulations, the initial mean velocity is prescribed by a hyperbolic tangent profile, as in Stanley, Sarkar & Mellado (2002), da Silva & Pereira (2008),

$$U(x, y, z) = \left(\frac{U_1 + U_2}{2}\right) + \alpha \left(\frac{U_1 - U_2}{2}\right) \tanh\left[\frac{H}{4\theta_0}\left(1 - \frac{2|y|}{H}\right)\right], \qquad (2.1)$$

where x, y, z are the streamwise, normal and spanwise jet/wake directions, respectively, θ_0 is the initial momentum thickness, and U_1 and U_2 are the maximum and minimum initial mean velocities, respectively. Planar jets are obtained by setting the constant α equal to $\alpha = 1$, whereas planar wakes are recovered with $\alpha = -1$. A three-component

https://doi.org/10.1017/jfm.2021.168 Published online by Cambridge University Press

velocity fluctuating 'spectral noise' (Lesieur, Ossia & Métais 1999) is superimposed by a convolution function that restricts the initial velocity noise to the initial shear layer region of the jet/wake.

The JET simulations used here correspond to two simulations described in Silva *et al.* (2018). In the simulations $U_1 = 1$ and $U_2 = 0$, and the ratio between the initial momentum thickness θ_0 and the jet initial width H is $H/\theta_0 = 35$. The several simulations essentially differ in the initial Reynolds number $Re_H = (U_1 - U_2)H/\nu$, which is equal to $Re_H = 8000$ and 12 000 for JET_{193} and JET_{276}, respectively, and on the number of collocation points used in the three spatial directions $(N_x \times N_y \times N_z)$, since the size of the computational domain is equal to $(7H \times 7H \times 3.5H)$ for both simulations, as well as the maximum amplitude of initial velocity fluctuations which is fixed at 5 % of the maximum velocity.

A total of three new temporal simulations of planar turbulent wakes were carried out in the present work (table 1), with an initial Reynolds number varying between $Re_H = (U_1 - U_2)H/\nu = 16\,000$ to 18 000, and with a computational domain extending to $(L_x, L_y, L_z) = (7H, 7H, 1.75H)$, and using a total of $(N_x \times N_y \times N_z) = (2048 \times 2048 \times 512)$ collocation points. The maximum amplitude of the velocity fluctuations was the same as used in the JET simulations, while the ratio H/θ_0 was set to 25 (different values of H/θ_0 have been used for the JET and WAKE simulations because of the marked differences observed in the evolution of these flows). The assessment of the new WAKE simulations is described in appendix A.

Using the data presented in table 1, one can estimate the range of the Kolmogorov micro-scales available from the present simulations, bearing in mind that some values in the table have been rounded. This can be done by computing $\eta = (\Delta x/\eta)^{-1}(L_x/N_x)$, which leads to $\eta = 0.0022$ and $\eta = 0.0041$ for the higher and smaller Reynolds numbers, respectively, so that the Kolmogorov micro-scale from the simulations used here vary by a factor of ≈ 2. We believe this range is enough to assess the scaling of the conditional statistics, particularly since the flow types analysed here is also very different.

2.2. *Conditional statistics in relation to the position of the TNTI*

In the present work, in order to isolate samples/data collected at particular locations within the TNTI layer, we use conditional statistics in relation to the distance from a specific position within the TNTI layer. This procedure has been extensively used in many previous works, and only a brief description will be given here.

The need to use these conditional statistics of course stems from the difficulty in obtaining adequate information about the dynamics of the TNTI layer when using classical statistics, i.e. computed at fixed locations within the flow domain. Because of the highly convoluted shape of the TNTI layer, together with its intermittent position, any such classical statistics will invariably contain samples corresponding both to IR and T flow events, thus masking the detailed local dynamics of turbulence within the TNTI layer.

The procedure used to obtain these conditional statistics follows three steps and is described in figure 1 (Silva *et al.* 2018): for obtaining conditional statistics in relation to the envelope of the irrotational boundary (IB) (i) the outer surface of the TNTI layer – the IB – which consists of an isosurface of very low vorticity magnitude $\omega_{th} = (\omega_i\omega_i)^{1/2}$, is detected by analysing a histogram of the turbulent flow fraction of the flow (Taveira & da Silva 2013); (ii) the local enstrophy gradient is then used to define a three-dimensional (3-D) normal at each point of the IB in the upper and lower shear layers that delimits the interface envelope (Westerweel *et al.* 2009) for each of the $N_x \times N_z$ points from the upper and lower TNTs; (iii) any flow quantity of interest is collected at fixed distances

https://doi.org/10.1017/jfm.2021.168 Published online by Cambridge University Press

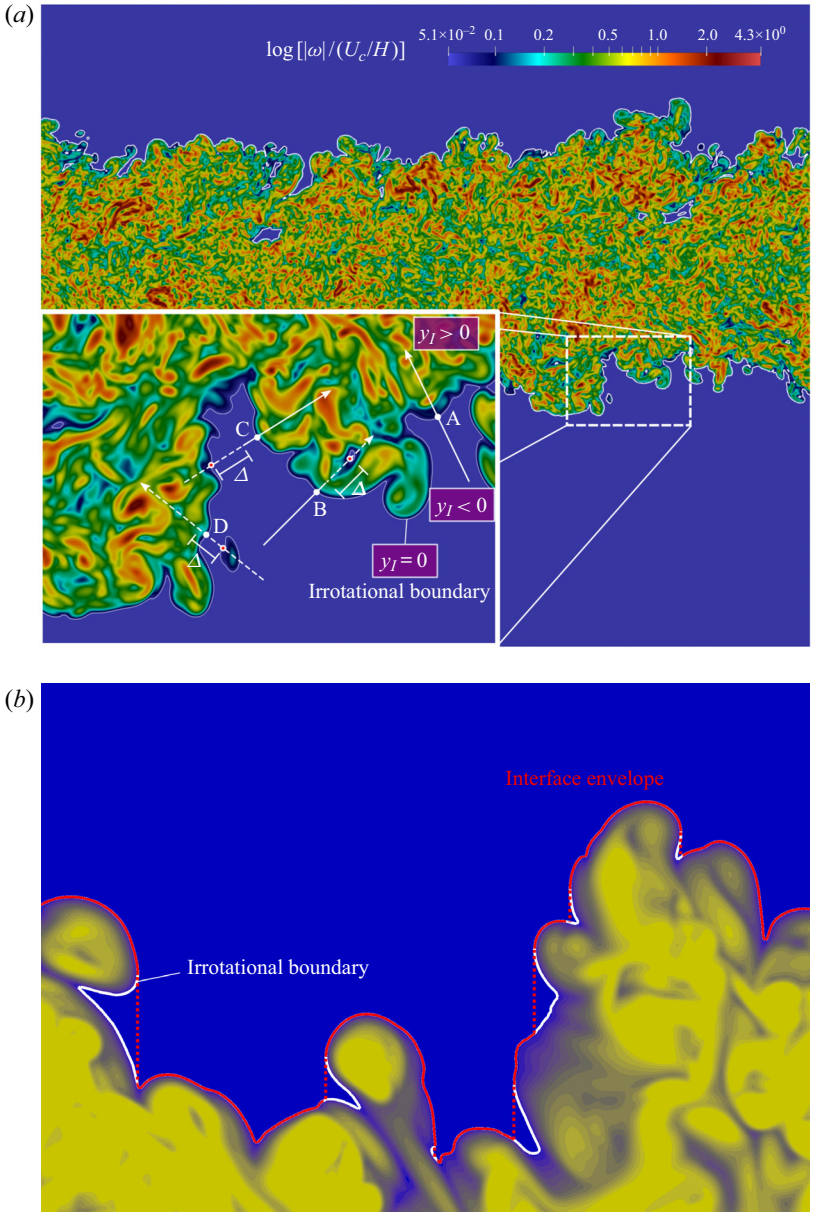

Figure 1. (*a*) Sketch of the procedure used to compute the conditional statistics in relation to the position of the IB or the interface enveloping the IB, showing contours of enstrophy in a (x, y) plane for the simulation JET_{193}, with an inset displaying a magnification of the region near the IB. The local axis at each point of the IB is used to collect data at fixed distances from the IB, y_I. The figure indicates also several points (B-D) involving different problems (see text for details). (*b*) Sketch of the region near the IB for the simulation JET_{193} showing the 'true' IB and the interface envelope.

y_I, by trilinear interpolation, into a grid defined on this local 3-D normal, that points into the interior of the turbulent core region, so that $y_I < 0$ and $y_I > 0$ correspond to the IR and T regions, respectively (the IB is located at $y_I = 0$). We denote the mean of a general quantity ϕ computed with this procedure as $\langle\phi\rangle_I$. The conditional statistics in relation to

https://doi.org/10.1017/jfm.2021.168 Published online by Cambridge University Press

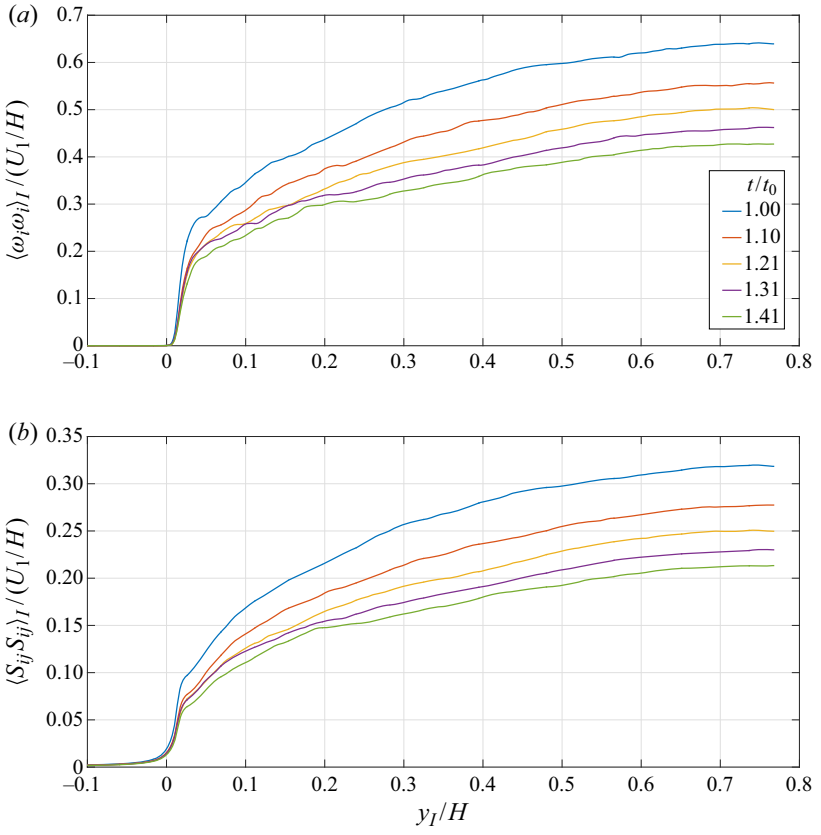

Figure 2. Conditional mean profiles of enstrophy $\langle\omega_i\omega_i\rangle_I$ (a) and strain magnitude $\langle S_{ij}S_{ij}\rangle_I$ (b) for the simulation WAKE$_{305}$ at several time instants during the flow decay at the far field regime. The enstrophy and strain magnitude are normalised by the initial free stream velocity U_1 and initial width of the wake H. The IB is located at $y_I = 0$, and the IR and T regions correspond to $y_I < 0$ and $y_I > 0$, respectively, and y_I is normalised by the thickness of the initial shear layer region H.

the local IB are obtained by simply replacing the envelope of the IB by the local IB in step (ii).

As in virtually all works using conditional analysis of the TNTI layer, here we use the interface envelope. Figure 1(a) shows the procedure used to compute the conditional statistics in relation to the IB position and indicates also several points (B-D) involving different problems. Following Westerweel *et al.* (2009), bubbles of IR flow inside the T region are discarded from the statistical sample (e.g. near point B). The same happens with islands of turbulent flow inside the NT region (e.g. near point D). Figure 1(b) shows the IB and the interface envelope, that discards several re-entrances from the statistical sample. In the present work and for each simulation, a single instantaneous field is used to compute the conditional statistics corresponding to each individual simulation, which is sufficient to obtain a good level of convergence of the desired quantities because of the large number of grid points used in each simulation.

Figures 2(a) and 2(b) illustrates the application of this procedure by showing conditional mean vorticity magnitude profiles $\langle\omega_i\omega_i\rangle_I$ and strain magnitude $\langle S_{ij}S_{ij}\rangle_I$, respectively, for WAKE$_{305}$ at different time instants. The distance y_I is normalised by the wake initial slot-width H and the mean vorticity magnitude and strain magnitude are normalised

https://doi.org/10.1017/jfm.2021.168 Published online by Cambridge University Press

by U_1/H. For all instants, the vorticity magnitude is virtually zero in the IR region and tends to a constant value inside the turbulent core region, after undergoing a very sharp vorticity jump right after the IB position ($0 \leq y_I/H \leq 0.025$). This sharp jump occurs within the TNTI layer, whereas the smaller vorticity increase observed afterwards ($0.025 \leq y_I/H \leq 0.3$) is associated to large-scale inhomogeneities within the turbulent core region (as will be discussed below). The decay of vorticity observed for increasing times is concomitant with the classical decay of the wake in the fully developed turbulent regime. The strain magnitude has a similar shape deep inside the T region, where $\langle\omega_i\omega_i\rangle_I \approx 2\langle S_{ij}S_{ij}\rangle_I$. An important difference between the two quantities can be observed in the IR region. Whereas the vorticity falls sharply to zero when approaching the IB and is zero in the NT region, the strain falls much more slowly and has non-negligible values inside this region (Holzner *et al.* 2007; Teixeira & da Silva 2012). The shape of these conditional profiles has been reported in many different shear flows, including jets, mixing layers and also in boundary layers (e.g. Bisset *et al.* 2002; Westerweel *et al.* 2005; Holzner *et al.* 2007; Watanabe *et al.* 2019).

The conditional Reynolds number listed in table 1, $\langle Re_\lambda\rangle_T$, is computed in the following way. We use conditional mean profiles of the viscous dissipation rate $\langle\varepsilon\rangle_I = 2\nu\langle S_{ij}S_{ij}\rangle_I$, and Taylor micro-scale $\langle\lambda\rangle_I = \sqrt{15\nu\langle u'^2\rangle_I/\langle\varepsilon\rangle_I}$, and with these we compute the conditional mean Taylor-based Reynolds number $\langle Re_\lambda\rangle_I = \sqrt{\langle u'^2\rangle_I}\langle\lambda\rangle_I/\nu$. Note that here $\langle u'^2\rangle_I = \langle u^2\rangle_I - \langle u\rangle_I^2$ since it has been shown that this is the correct way to compute the conditional Reynolds stresses (Bisset *et al.* 2002; Westerweel *et al.* 2005; Taveira & da Silva 2013). The particular values listed in table 1 correspond to the turbulent core region, far away from the TNTI layer, and were computed at a distance of $y_I/\eta \approx 250$ for all simulations, i.e. $\langle Re_\lambda\rangle_T = \langle Re_\lambda\rangle_I(y_I/\eta = 250)$. Finally, we want to stress that in the following text the instantaneous Kolmogorov length and velocity scales, which appear often in the discussion, are never actually computed on a local and instantaneous basis. When these scales are mentioned they imply a given averaging operation, i.e. $u_\eta \equiv \langle u_\eta\rangle$, where the brackets indicate some sort of averaging, e.g. $u_\eta = \langle u_\eta\rangle_T = \langle(\nu\varepsilon)^{1/4}\rangle_T$.

3. Results and discussion

This section shows that the small-scale quantities of the flow within the TNTI layer, as obtained from very different flow types (SFT, JET, WAKE), are universal when plotted with the appropriate normalisation. Specifically, we show that the statistics of the enstrophy and strain, and of their governing equation terms, as well as the invariants of the velocity gradient tensor, such as the conditional means and joint probability density functions, all collapse into the same curves when normalised by the mean local Kolmogorov (velocity and length) scales.

3.1. *Universality of the normalised conditional mean enstrophy profiles*

When analysing the dynamics of the flow in the vicinity and within the TNTI layer, the vorticity magnitude $|\boldsymbol{\omega}| = (\omega_i\omega_i)^{1/2}$ or, alternatively, the enstrophy $\omega = \omega_i\omega_i/2$ are key important quantities since in the IR (or NT) region $|\boldsymbol{\omega}| = \omega = 0$, whereas in the T region $|\boldsymbol{\omega}| \neq 0$ (and $\omega \neq 0$), so that the evolution of these quantities is an important measure of the transition of the flow from the NT into the T region, and can be used to quantify the small-scale features of the entrainment process ('nibbling'). In the present work, enstrophy is defined by $\omega = \omega_i\omega_i$, instead of the definition $\omega = \omega_i\omega_i/2$ used by some authors. Without loss of generality, the definition of enstrophy as $\omega = \omega_i\omega_i/2$ is only used

https://doi.org/10.1017/jfm.2021.168 Published online by Cambridge University Press

in connection with the conditional budgets across the TNTI layer, which are analysed in § 3.2.

As described in the introduction, conditional mean profiles of both $|\boldsymbol{\omega}|$ and ω, with minor differences in the averaging procedure, have been obtained in many experimental and numerical works, where the normalisation has been done in several different ways (Silva *et al.* 2018). In earlier investigations of the TNTI layer the normalisation was typically done using the flow parameters (e.g. initial/outer characteristic scales), as in figure 2 of the present work, or using large-scale flow parameters (e.g. centreline mean velocity, half-width, integral scale) (Bisset *et al.* 2002). However, it is difficult to compare conditional mean profiles using these quantities and many authors have used either the Taylor scale or the Kolmogorov micro-scale, computed at some suitable location, to normalise the distances within the TNTI layer. In light of recent developments the normalisation of the distances with the Kolmogorov micro-scale makes more sense, since the thickness of the TNTI layer scales with this scale at high Reynolds numbers (Silva *et al.* 2018), and this normalisation has been used in many recent works (e.g. Watanabe *et al.* 2018; Breda & Buxton 2019). In these cases the reference Kolmogorov scales are taken from a region inside the turbulent core region of the flow, adjacent to the TNTI layer. Figures 3(*a*) and 3(*b*) show conditional mean profiles of the Kolmogorov micro-scale η and of the Kolmogorov velocity $u_\eta = (\nu\varepsilon)^{1/4}$, respectively, for all the simulations used in the present work. It is clear that at a distance relatively close to the TNTI layer ($y_I/\langle\eta\rangle_T \gtrsim 60$–$70$), both the Kolmogorov micro-scale and the Kolmogorov velocity are virtually constant and equal to the value measured inside the turbulent core region, i.e. $\langle\eta\rangle_I/\langle\eta\rangle_T = 1.0$, for $y_I/\langle\eta\rangle_T >> 1$ (recall that the thickness of the TNTI layer is $\langle\delta_\omega\rangle/\langle\eta\rangle_T \approx 15$). The Kolmogorov scale has no meaning outside the T region ($y_I/\langle\eta\rangle_T \leq 0$) and, even within the VSL region of the TNTI layer ($y_I/\langle\eta\rangle_T \lesssim 5$), changes only slightly over the entirety of the flow, displaying a maximum at the IB ($y_I/\langle\eta\rangle_T = 0$) of $\langle\eta\rangle_I/\langle\eta\rangle_T \approx 1.5$, the observed variation (50 %) happening only in the smallest possible space, in a fraction of the VSL, which typically has a size of about $\approx 5\eta$. Otherwise, the Kolmogorov micro-scale (like the Kolmogorov velocity scale) is virtually constant in the entirety of the turbulent region i.e. for $y_I > 0$.

Thus, the normalisation of the conditional mean enstrophy profiles by the Kolmogorov (velocity and length) scales is justified by the uniform value these quantities take in the turbulent core region near the TNTI layer, and by the recently observed Kolmogorov scaling of this interface and its sublayers at high Reynolds numbers.

Figure 4 compares the mean conditional enstrophy profiles normalised by the reference (turbulent core) Kolmogorov velocity and length scales, $\langle\omega_i\omega_i\rangle_I/(\langle u_\eta\rangle_T/\langle\eta\rangle_T)^2$, for all the simulations used in the present work. As in da Silva & Pereira (2008), Silva *et al.* (2018), Holzner *et al.* (2008, 2009), Watanabe *et al.* (2018), the Kolmogorov scales used for the normalisation are taken from deep inside the turbulent region (here the reference values are taken at $y_I/\langle\eta\rangle_I = 250$).

This comparison between the conditional mean profiles of enstrophy has seldom been done using data from completely different flow types. The compilation of conditional mean vorticity and enstrophy profiles shown in figure 6 in da Silva *et al.* (2014) is not a fair comparison because of differences in the data (enstrophy, spanwise vorticity, vorticity magnitude) and the details of the procedure used to obtain the conditional statistics (e.g. using a one-dimensional vertical line, two-dimensional normal, 3-D normal). More importantly, the Reynolds numbers of some of these simulations were simply too low, as the analysis of interface thickness scaling described in Silva *et al.* (2018) has shown.

https://doi.org/10.1017/jfm.2021.168 Published online by Cambridge University Press

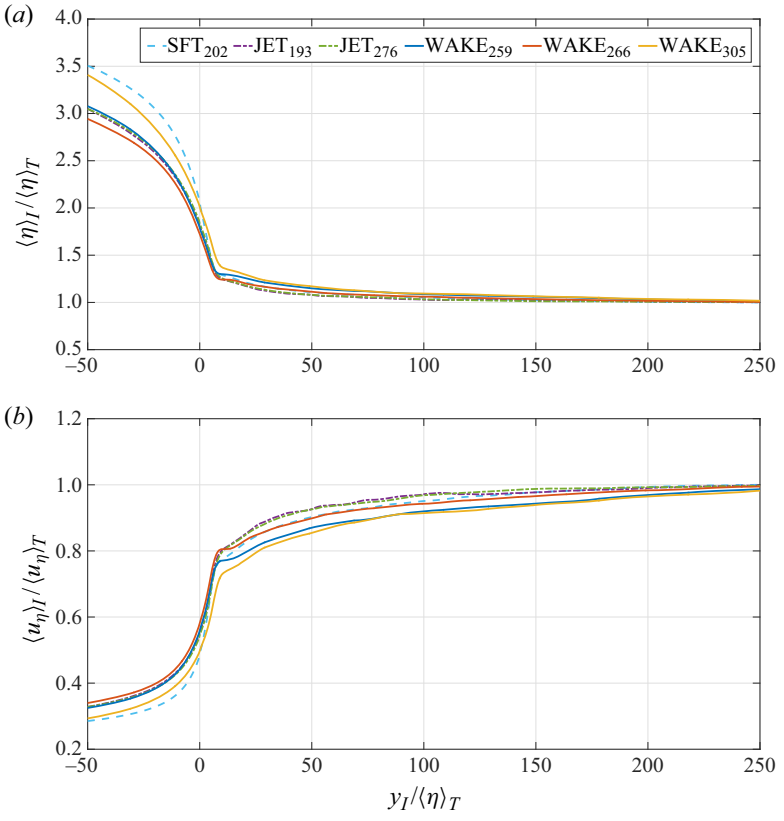

Figure 3. Conditional mean profiles of Kolmogorov micro-scale $\langle\eta\rangle_I$ (*a*) and Kolmogorov velocity $\langle u_\eta\rangle_I$ (*b*) for all the simulations considered in this work, normalised by their mean values at the turbulent core region of the flow, $\langle\eta\rangle_T$ and $\langle u_\eta\rangle_T$, respectively. The distance from the IB (y_I) is normalised with the mean Kolmogorov micro-scale computed at the turbulent core region, $\langle\eta\rangle_T$. (*a*) Conditional mean Kolmogorov micro-scale $\langle\eta\rangle_I$ and (*b*) conditional mean Kolmogorov velocity $\langle u_\eta\rangle_I$.

The curves in Figure 4 are somehow similar, with a sharp enstrophy jump after the IB position, followed by a slow rise into the turbulent core region. However, it is clear that the conditional profiles do not collapse because of differences in the normalised enstrophy magnitude and the way the enstrophy moves into the turbulent core region, i.e. different magnitudes of the profiles at a given distance $y_I/\langle\eta\rangle_T$ from the IB position. The thickness of the vorticity jump is of course of the same order in all cases, with $\langle\delta_\omega\rangle/\langle\eta\rangle_T \approx 10$–$20$, in agreement with Silva *et al.* (2018). The different evolution of the enstrophy for $y_I/\langle\eta\rangle_T \gg 20$, i.e. large distances from the IB is connected with large-scale inhomogeneities within the flow and not with the dynamics of the flow within the TNTI layer (as will be shown below), as it is unlikely that the small-scale dynamics at the interface can be affected by small-scale events taking place at distances of more than 200 Kolmogorov micro-scales away. The approach towards $\langle\omega_i\omega_i\rangle_I/(\langle u_\eta\rangle_T/\langle\eta\rangle_T)^2 \to 1$ for $y_I/\langle\eta\rangle_T \gg 1$ is explained by kinematic constraints, since in the turbulent core region $\langle\omega_i\omega_i\rangle/\langle(u_\eta/\eta)^2\rangle = 1$, as in homogeneous turbulence.

The non-collapsing nature of the profiles of conditional mean enstrophy for different flows, or even for the same flow at different Reynolds numbers, when these profiles are normalised by a reference Kolmogorov velocity and length scale, has been reported before

https://doi.org/10.1017/jfm.2021.168 Published online by Cambridge University Press

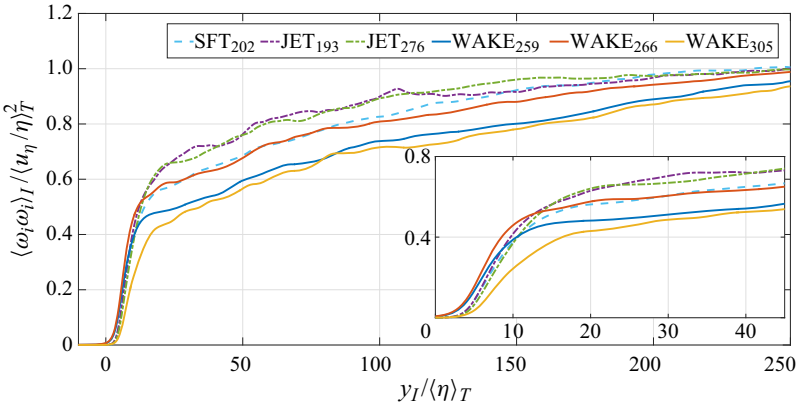

Figure 4. Conditional mean enstrophy profile $\langle\omega_i\omega_i\rangle_I$ for all the simulations considered in this work, normalised with the mean Kolmogorov velocity and length scale, computed at the turbulent core region of the flow, $\langle\eta\rangle_T$ and $\langle u_\eta\rangle_T$, respectively. The inset shows the amplified region near the IB ($y_I = 0$).

in several works; see, e.g. figures 5 and 16(*b*) of Watanabe, Nagata & da Silva (2017*b*), Watanabe *et al.* (2018), respectively. The particular shape of these mean enstrophy profiles can be justified by the simple arguments described in appendix B.

In light of the above discussion, since the Kolmogorov velocity, length (and, therefore, time) scales are clearly the characteristic scales of the TNTI layer, it is natural to normalise all small-scale quantities with the mean local Kolmogorov scales, i.e. to plot $\langle\omega_i\omega_i\rangle_I$ normalised by $(\langle u_\eta\rangle_I/\langle\eta\rangle_I)^2$, as shown in figure 5. In contrast to figure 4, here all the conditional enstrophy profiles collapse nicely into a single curve. That the collapse is indeed perfect can be attested by the very small separation distance between the individual curves, which is comparable to the resolution of the simulations, of the oder of one Kolmogorov micro-scale. As before, the normalised enstrophy tends to $\langle\omega_i\omega_i\rangle_I/(\langle u_\eta\rangle_I/\langle\eta\rangle_I)^2 = 1$ away from the TNTI layer, but unlike in figure 4, here this value is attained very quickly, at $y_I/\langle\eta\rangle_I \approx 30$, which is shortly after the end of the TNTI layer, which extends at most until $y_I/\langle\eta\rangle_I \approx 20$. Inside the TNTI layer, again in marked contrast to figure 4, the normalised enstrophy exhibits a peak that reaches $\langle\omega_i\omega_i\rangle_I/(\langle u_\eta\rangle_I/\langle\eta\rangle_I)^2 \approx 1.3$, and is located at $y_I/\langle\eta\rangle_I \approx 15$. Close to the IB the normalised enstrophy displays a very sharp rise, as in figure 4. Note that the conditional profile of $\langle\omega_i\omega_i/(u_\eta/\eta)^2\rangle_I$ is theoretically 'similar' but is affected by considerably more intermittency, and, therefore, would need more samples/instants to attain an equivalent degree of convergence. The use of the local Kolmogorov scales to normalise the enstrophy can be questioned at first sight because the definition of these scales arises from the classical description of the energy cascade mechanism, which does not take place very close to the IB (Watanabe *et al.* 2019); however, it can also be argued that the Kolmogorov scales are a natural definition of the viscous scales at work within the flow, and in this sense, the variable Kolmogorov scales near the IB have a clear physical meaning. Appendix C shows that the spatial or temporal nature of the simulations/flow type does not affect the present results; Reynolds number effects are discussed in appendix D.

The shape of the normalised enstrophy depicted in figure 5 and, in particular, the deviation from the asymptotic value of 1 can be understood as a consequence of a deviation of the flow from local homogeneity near the TNTI layer. To see this, consider the expansion

https://doi.org/10.1017/jfm.2021.168 Published online by Cambridge University Press

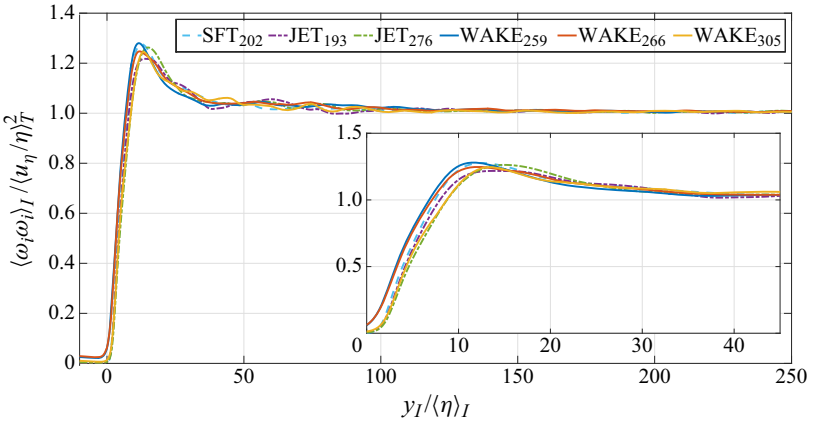

Figure 5. Conditional mean enstrophy profile $\langle\omega_i\omega_i\rangle_I$ for all the simulations considered in this work, normalised with the mean local Kolmogorov velocity and length scale, computed at each coordinate y_I, $\langle\eta\rangle_I$ and $\langle u_\eta\rangle_I$, respectively. The inset shows the amplified region near the IB ($y_I = 0$).

of the enstrophy and the normalising Kolmogorov velocity and length scale ratio, i.e.

$$\omega_i\omega_i = \epsilon_{ijk}\frac{\partial u_k}{\partial x_j}\epsilon_{ilm}\frac{\partial u_m}{\partial x_l} = \left(\frac{\partial u_k}{\partial x_j}\right)^2 - \frac{\partial u_k}{\partial x_j}\frac{\partial u_j}{\partial x_k} \tag{3.1}$$

and

$$\left(\frac{u_\eta}{\eta}\right)^2 = \frac{\varepsilon}{\nu} = 2S_{ij}S_{ij} = \frac{1}{2}\left(\frac{\partial u_i}{\partial x_j} + \frac{\partial u_j}{\partial x_i}\right)^2 = \left(\frac{\partial u_i}{\partial x_j}\right)^2 + \frac{\partial u_i}{\partial x_j}\frac{\partial u_j}{\partial x_i}. \tag{3.2}$$

Using the above relations, the conditional mean enstrophy normalised by the local Kolmogorov scales can be written as

$$\frac{\langle\omega_i\omega_i\rangle_I}{\left\langle\frac{u_\eta^2}{\eta^2}\right\rangle_I} = \frac{\left\langle\left(\frac{\partial u_i}{\partial x_j}\right)^2\right\rangle_I - \left\langle\frac{\partial u_i}{\partial x_j}\frac{\partial u_j}{\partial x_i}\right\rangle_I}{\left\langle\left(\frac{\partial u_i}{\partial x_j}\right)^2\right\rangle_I + \left\langle\frac{\partial u_i}{\partial x_j}\frac{\partial u_j}{\partial x_i}\right\rangle_I}. \tag{3.3}$$

For an homogeneous incompressible flow,

$$\left\langle\frac{\partial u_i}{\partial x_j}\frac{\partial u_j}{\partial x_i}\right\rangle_I = \frac{\partial}{\partial x_j}\left\langle u_i\frac{\partial u_j}{\partial x_i}\right\rangle_I = 0, \tag{3.4}$$

and, therefore, the ratio in (3.3) is only different from 1 in flow regions where the flow is not (locally) homogeneous. Figure 5 therefore shows that, for $y_I/\langle\eta\rangle_I \lesssim 35$, which already covers a small region outside the TNTI layer, the flow is locally inhomogeneous. This result is interesting because it shows that there is a length of about 10η, outside the TNTI layer, where the small-scale features of the flow are already characteristic of the turbulent core region, i.e. the flow is still adjusting from the presence of the nearby TNTI layer.

The value of $\langle\omega_i\omega_i\rangle_I/\langle(u_\eta/\eta)^2\rangle_I > 1$ observed for $10 \lesssim y_I/\langle\eta\rangle_I \lesssim 35$ can be explained by the bigger density of intense vortices here compared with inside the turbulent core region of the flow, because the IB is defined around these structures

https://doi.org/10.1017/jfm.2021.168 Published online by Cambridge University Press

(da Silva *et al.* 2011; Watanabe *et al.* 2017*a*). Indeed, (3.3) implies that a region with values of the normalised conditional enstrophy with $\langle\omega_i\omega_i\rangle_I/\langle(u_\eta/\eta)^2\rangle_I > 1$ is only possible if $\langle(\partial u_i/\partial x_j)(\partial u_j/\partial x_i)\rangle_I < 0$ in those regions. This term can be related to the Laplacian of conditional mean pressure $\langle p\rangle_I$, through the Poisson equation,

$$\nabla^2\langle p/\rho\rangle_I = -\left\langle \frac{\partial u_i}{\partial x_j}\frac{\partial u_j}{\partial x_i}\right\rangle_I, \tag{3.5}$$

where ρ is the (constant) flow density. Therefore, the observed maximum of $\langle\omega_i\omega_i\rangle_I/\langle(u_\eta/\eta)^2\rangle_I$ indicates the existence of a mean (local) pressure minimum. The conditional mean profile of $\langle\nabla^2 p\rangle_I$ can be also connected with the second invariant of the velocity gradient tensor $Q = \frac{1}{4}(\omega_i\omega_i - 2S_{ij}S_{ji})$, since $\nabla^2 p = 2Q$ (Davidson 2004). Conditional mean profiles of $\langle Q\rangle_I$, normalised with the Kolmogorov micro-scales at the turbulent core region, are shown in figure 6(*a*) for all the simulations used in the present work. These profiles are similar to that shown in da Silva & Pereira (2008, 2009), and show the existence of double (positive/negative) peaks of Q associated with a predominance of enstrophy/strain near the IB position in the T and NT regions, respectively. The mean value of $\langle Q\rangle_I = 0$ observed in the turbulent core and irrotational core regions is again explained by the homogeneity of the flow in these regions.

Figure 6(*b*) shows the same profiles normalised with the local mean Kolmogorov scales, again showing a better collapse of all the curves and the emergence of the universal shape of the conditional Q in the TNTI layer. The maximum is $\langle Q\rangle_I/\langle(u_\eta/\eta)^2\rangle_I \approx 0.06$ and is located at the same location corresponding to the maximum of $\langle\omega_i\omega_i\rangle_I/\langle(u_\eta/\eta)^2\rangle_I$, while the value of $< Q >_I /\langle(u_\eta/\eta)^2\rangle_I \approx -1/4$ observed in the IR region is simply a consequence of the definition of Q in a region of zero enstrophy, and of the scaling of strain $S_{ij}S_{ij} \sim (u_\eta/\eta)^2$. The conditional mean profiles of the third invariant of the velocity gradient $R = -1/3(S_{ij}S_{jk}S_{ki} - 3/4\omega_i\omega_j S_{ij})$ (not shown) display similar trends, i.e. while the conditional mean profiles of $\langle R\rangle_I$ obtained from the several simulations normalised with the Kolmogorov scales from the turbulent core region display considerable differences, the same profiles normalised with the local Kolmogorov scales exhibit the same universal profile in all the simulations used in the present work.

It is clear that the particular shape of $\langle\omega_i\omega_i\rangle_I/\langle(u_\eta/\eta)^2\rangle_I$ and $\langle Q\rangle_I/\langle(u_\eta/\eta)^2\rangle_I$ is a consequence of the local low pressure associated with the presence of a large number of eddies, because the IB is defined by the flow eddies bounding the TNTI layer, and by their particular alignment (tangential to this layer), as shown in numerous works, e.g. da Silva *et al.* (2011), Mistry, Philip & Dawson (2019).

The results presented so far are related, totally or in part, to the vorticity (or the enstrophy), but it is important to show that the observed universality is also present in the rate-of-strain tensor, which is another important small-scale turbulence quantity. Figure 7 shows the conditional mean rate-of-strain magnitude $\langle S_{ij}S_{ij}\rangle_I$, normalised in the usual way, i.e. with the reference Kolmogorov velocity and length scales from the turbulent core region. Clearly with this normalisation no universality can be observed, as the several profiles are different within the TNTI layer and beyond, even for $y_I/\langle\eta\rangle_T \gtrsim 250$. That this fact is associated with the effects of the large-scale inhomogeneities of the flow near the TNTI layer is easily shown by writing

$$\langle S_{ij}S_{ij}\rangle_I = \frac{1}{2\nu}\left\langle \frac{C_\varepsilon u'^3}{L}\right\rangle_I, \tag{3.6}$$

https://doi.org/10.1017/jfm.2021.168 Published online by Cambridge University Press

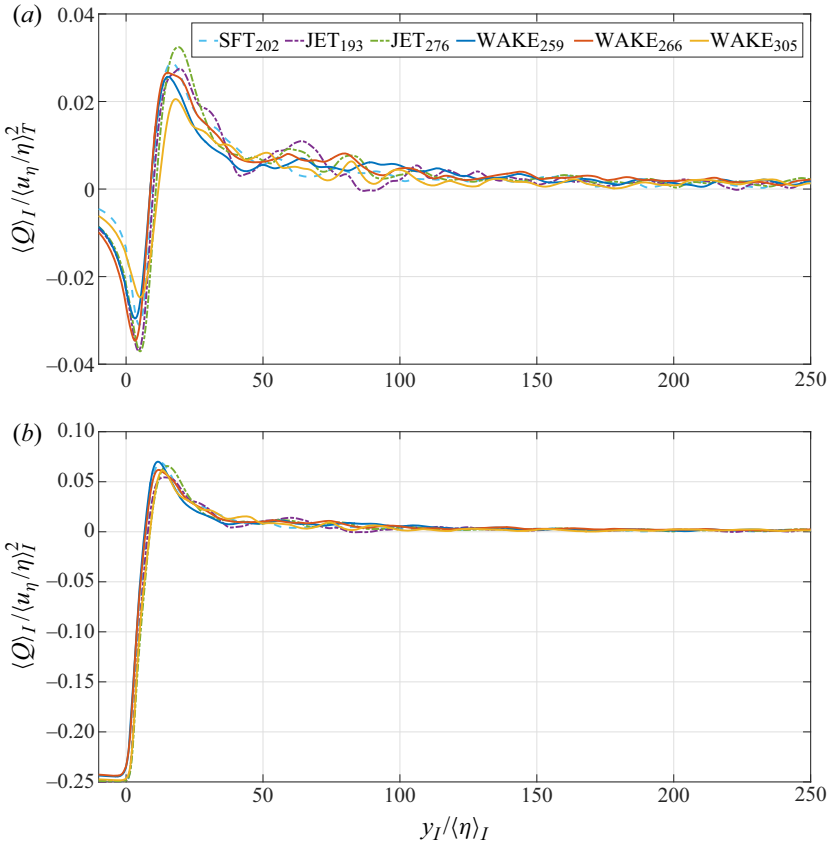

Figure 6. Normalised conditional mean profiles of the second invariant of the velocity gradient tensor $\langle Q\rangle_I$ for all the simulations used in the present work, normalised with the reference Kolmogorov scales (*a*) and with the local Kolmogorov scales (*b*).

where the non-dimensional dissipation $C_\varepsilon = \varepsilon L/u'^3$ is defined with the integral scale of turbulence L and the root mean square of the velocity fluctuations u'. Since, as shown by Watanabe *et al.* (2019), both C_ε and L are approximately constant for $y_I/\langle\eta\rangle_T \gtrsim 15$, the continuous rise of $\langle S_{ij}S_{ij}\rangle_I$ observed in figure 7 must be explained by variations of the Reynolds stresses when moving away from the IB position. However, the universality or the rate-of-strain magnitude, $S_{ij}S_{ij}$, (and of the viscous dissipation rate ε) when using the local normalisation is trivially demonstrated from (3.2),

$$\frac{\langle S_{ij}S_{ij}\rangle_I}{\langle(u_\eta/\eta)\rangle_I^2} = \frac{1}{2} \tag{3.7}$$

for all y_I (including the NT region), i.e. the mathematical definition of the Kolmogorov velocity and length scales implies the similarity of the rate-of-strain magnitude, when normalised with the local mean Kolmogorov scales. This has been confirmed for all the simulations used in the present work (not shown), and explains also why $\langle S_{ij}S_{ij}\rangle_I$ in figure 7 (normalised with the turbulent core Kolmogorov scales) is seen approaching the constant $1/2$ as $y_I/\langle\eta\rangle_T$ increases.

It is noteworthy that the perfect collapse observed above for the conditional means of the vorticity and strain (and related small-scale quantities – see below) is not observed

https://doi.org/10.1017/jfm.2021.168 Published online by Cambridge University Press

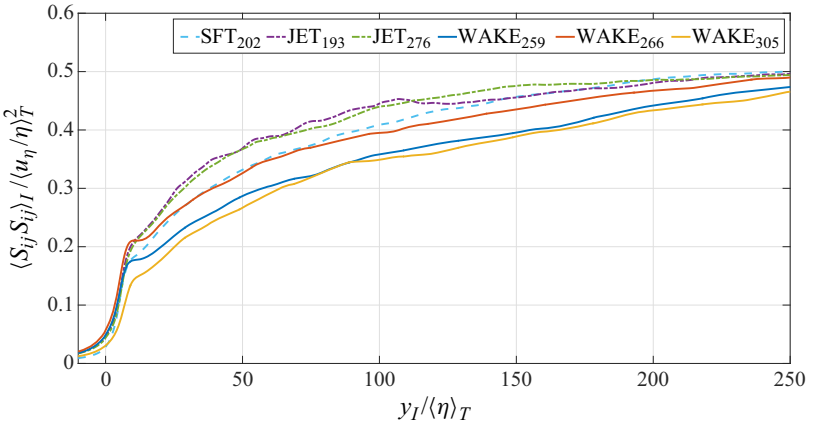

Figure 7. Normalised conditional mean profiles of the rate-of-strain magnitude $\langle S_{ij}S_{ij}\rangle_I$ for all the simulations used in the present work, normalised with the mean Kolmogorov velocity and length scale, computed at the turbulent core region of the flow, $\langle\eta\rangle_T$ and $\langle u_\eta\rangle_T$, respectively.

for typical large-scale quantities. As expected, the conditional Reynolds stresses (when normalised with the local Kolmogorov scales) do not collapse into the same curve. On the contrary, very different curves are obtained for these statistics, even for different instants of the same flow, except right at the IB (not shown).

The degree to which the small scales of turbulence can satisfy the classical isotropic turbulence statistics can be appreciated by analysing the skewness of the longitudinal velocity gradient, S_0, defined by Davidson (2004),

$$S_0 = \left\langle \left(\frac{\partial u'}{\partial x}\right)^3 \right\rangle \Bigg/ \left\langle \left(\frac{\partial u'}{\partial x}\right)^2 \right\rangle^{3/2}, \tag{3.8}$$

where the averaging is performed in the homogenous directions of the flow, and is strongly linked to the production of enstrophy,

$$\langle \omega_i\omega_j S_{ij}\rangle = -\frac{7}{6\sqrt{15}} S_0 \langle \omega_i\omega_i\rangle^{3/2}. \tag{3.9}$$

Clearly, a negative value of S_0 is necessary for the mean of the enstrophy production to be positive, as is always the case in fully developed turbulence (Davidson 2004). Ishihara *et al.* (2007) showed that S_0 is approximately constant, with only a mild-Reynolds-number dependence ($0.51 \lesssim -S_0 \lesssim 0.67$ for $200 \lesssim Re_\lambda \lesssim 300$).

Figure 8 shows the mean conditional S_0 for all the simulations used in the present work, computed as

$$\langle S_0\rangle_I = -\frac{6\sqrt{15}}{7}\frac{\langle \omega_i\omega_j S_{ij}\rangle_I}{\langle \omega_k\omega_k\rangle_I^{3/2}}. \tag{3.10}$$

Here $\langle S_0\rangle_I$ is constant in the turbulent core and has the same value moving into the TNTI layer until about $y_I/\langle\eta\rangle_I \approx 20$–$30$ where it displays a small increase. The inset shows that values of $\langle S_0\rangle_I$ are between $0.52 \lesssim -S_0 \lesssim 0.62$, in good agreement with the isotropic values given the degree of convergence of the profiles. These profiles contrast with some conclusions of Breda & Buxton (2019) and show that the small scales of the flow can be represented by classical isotropic relations impressively close to the IB.

https://doi.org/10.1017/jfm.2021.168 Published online by Cambridge University Press

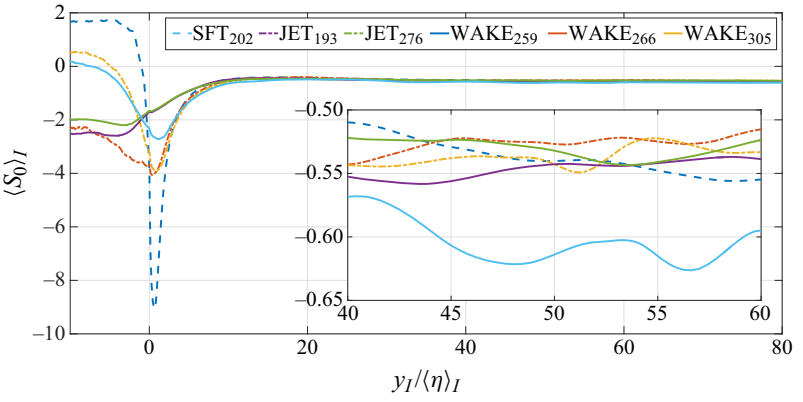

Figure 8. Conditional mean profile of the skewness of the velocity gradient $\langle S_0 \rangle_I$ for all the simulations considered in this work, where the distance to the IB ($y_I = 0$) is normalised by the mean local Kolmogorov scale $y_I/\langle \eta \rangle_I$, and the inset shows the amplified region near the IB.

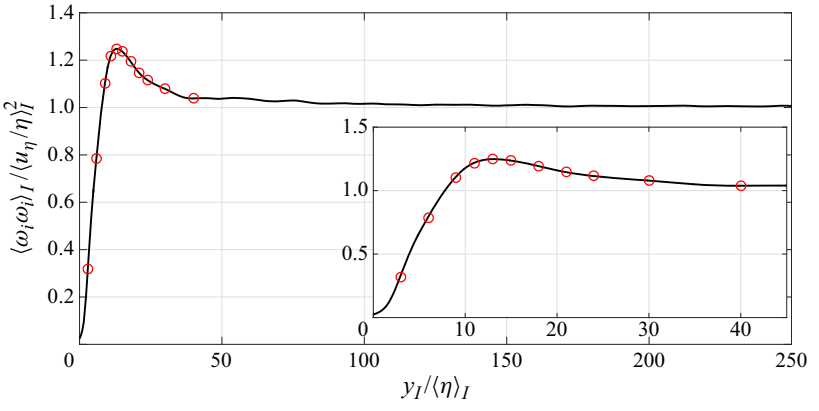

Figure 9. The self-similar conditional mean enstrophy profile $\langle \omega_i \omega_i \rangle_I$ normalised with the local Kolmogorov velocity and length scale, $\langle \eta \rangle_I$ and $\langle u_\eta \rangle_I$, respectively, obtained by averaging all the curves displayed in figure 5. The inset shows the amplified region near the IB ($y_I = 0$).

Finally, in order to document the universal shape of the normalised conditional mean enstrophy displayed in figure 5, we have averaged all the profiles in this figure. Figure 9 shows the resulting 'averaged' mean profile, and table 2 lists some of its coordinates for future reference. This profile of normalised conditional mean enstrophy is possibly a self-similar solution of a (locally) normalised enstrophy equation budget. Since this profile is virtually equal for the three very different flow types analysed here, a similar mean conditional enstrophy profile should be observed in virtually all Newtonian and incompressible TNTI layers. For completeness, appendix E discusses the small differences one gets when using the interface defined by the local IB introduced in § 2.2, instead of the envelope that is used throughout the present work.

We end this section with a small consideration on the importance of the results described above. Indeed, all the results convincingly show that the (mean) local Kolmogorov velocity and length scales are the natural scales characterising the conditional profiles of several small-scale quantities within the TNTI layer. At first sight one might be tempted to think that this is a trivial result since (i) it is well known that in fully developed turbulence the

https://doi.org/10.1017/jfm.2021.168 Published online by Cambridge University Press

$y_I/\langle\eta\rangle_I$	3	6	9	11	13	15	18	21	24	30	40
$\langle\omega_i\omega_i\rangle_I/\langle u_\eta/\eta\rangle_I^2$	0.317	0.785	1.103	1.217	1.248	1.237	1.195	1.147	1.116	1.080	1.038

Table 2. Coordinates of the self-similar conditional enstrophy profile $\langle\omega_i\omega_i\rangle_I/\langle u_\eta/\eta\rangle_I^2$, obtained by averaging over all the conditional enstrophy profiles in figure 5.

characteristics of the small scales of motion can be linked to the Kolmogorov micro-scale, e.g. the production of enstrophy can be estimated as $\omega_i\omega_j S_{ij} \sim (u_\eta/\eta)^3$, and (ii) it has recently been shown, in agreement with (i), that the thickness of the TNTI layer scales with the Kolmogorov micro-scale at sufficiently high Reynolds numbers.

However, we believe this is not a trivial result for two main reasons. First, the very definition of the Kolmogorov scales arises from the concept of an ongoing energy cascade, which is clearly atypical within the TNTI layer, as recently shown in Watanabe *et al.* (2019). In short, the small scales are strongly depleted in a big part of the TNTI layer, and are strongly unbalanced (in relation to the energy flux they receive from the large scales). Moreover, the non-dimensional dissipation C_ε displays anomalous power laws $C_\varepsilon \sim Re_\lambda^\alpha$ within the TNTI layer (Watanabe *et al.* 2019). Furthermore, the flow within the VSL is clearly not characteristic of fully developed turbulence, because viscosity strongly dominates this flow region no matter how high the Reynolds number may be. The second reason has to do with the supposed link between enstrophy $\rightarrow$ velocity gradients $\rightarrow$ viscous dissipation. Although this link certainly exists in a statistical sense in homogeneous turbulence, locally the relation between vorticity and strain is rather complex, as described at length in Tsinober, Ortenberg & Shtilman (1999), Tsinober (2019), and, moreover, the TNTI layer has distinct regions where it cannot be considered to be homogeneous. In short, enstrophy and strain are locally quite different, and this is even more so within the TNTI layer, where the flow is not statistically homogeneous.

To summarise, one should remember that the thickness of the TNTI layer is associated with just one feature of the conditional enstrophy profile in the TNTI layer (the length of the vorticity jump or the location of its peak), while present analysis of the conditional enstrophy profile focuses on the Kolmogorov scaling along the entirety of this profile. In this sense, the recent results demonstrating the Kolmogorov scaling of the TNTI thickness can be seen as a particular result encompassed in the present results on the shape of the conditional enstrophy profiles.

3.2. *Universality of conditional mean enstrophy budgets*

We now move into the analysis of the conditional mean enstrophy budgets. Applying a conditional mean at the enstrophy transport equation, the conditional mean enstrophy budget is written as

$$\underbrace{\left\langle \frac{D\omega^2/2}{Dt} \right\rangle_I}_{\text{Total variation, } T_\omega} = \underbrace{\langle\omega_i\omega_j S_{ij}\rangle_I}_{\text{Production, } P_\omega} + \underbrace{\langle\nu\nabla^2(\omega^2/2)\rangle_I}_{\text{Diffusion, } D_\omega} - \underbrace{\langle\nu\boldsymbol{\nabla}\omega_i\cdot\boldsymbol{\nabla}\omega_i\rangle_I}_{\text{Dissipation, } E_\omega}, \tag{3.11}$$

where the left-hand side represents the total variation of enstrophy (T_ω), whereas the terms on the right-hand side represent the production (P_ω), viscous diffusion (D_ω) and viscous dissipation (E_ω), respectively. Note that the application of this averaging procedure

https://doi.org/10.1017/jfm.2021.168 Published online by Cambridge University Press

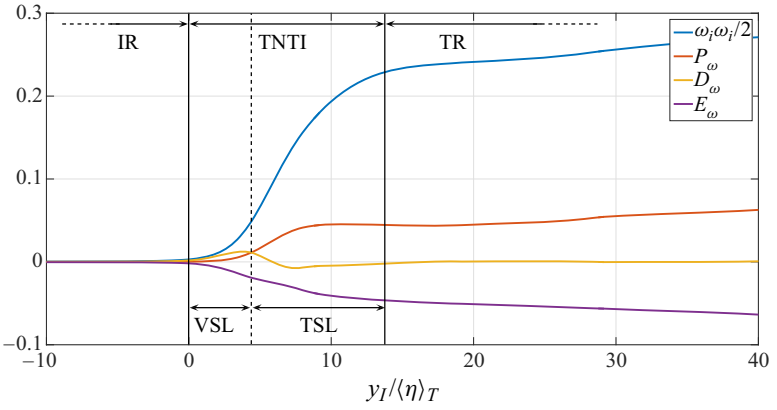

Figure 10. Conditional mean enstrophy budgets (3.11) for WAKE$_{259}$, normalised with the mean Kolmogorov velocity and length scale, computed at the turbulent core region of the flow, $\langle\eta\rangle_T$ and $\langle u_\eta\rangle_T$, respectively: enstrophy production (P_ω), enstrophy diffusion (D_ω) and enstrophy dissipation (E_ω). The figure also displays the location of the VSL and the TSL, which comprise the TNTI layer, separating the NT (or IR) and the turbulent core (TR) regions.

assumes that the IB moves at constant speed, otherwise, new terms would have to be added to this conditionally averaged equation, as discussed in Westerweel *et al.* (2009). This assumption is somehow consistent with the very small values observed for the local IB velocity (Holzner *et al.* 2009; Watanabe *et al.* 2014). The shape of these terms within the TNTI layer has been analysed in detail in numerous works (e.g. Bisset *et al.* 2002; Holzner *et al.* 2008; Taveira & da Silva 2014; Watanabe *et al.* 2016*b*). Figure 10 shows the conditional mean terms for WAKE$_{259}$ normalised in the usual way, i.e. using the reference Kolmogorov variables taken from the turbulence core region (very far from the IB) to normalise the whole conditional profiles.

The VSL consists of a subregion where viscous diffusion D_ω dominates the enstrophy growth within the TNTI layer ($D_\omega > P_\omega$), while in the TSL the enstrophy growth is dominated by the enstrophy production ($D_\omega < P_\omega$). The total extent of the TNTI layer (sum of the VSL and TSL) goes from the IB ($y_I/\eta = 0$) until the point at which enstrophy ceases to grow steeply ($y_I/\langle\eta\rangle \approx 15$), and separates the IR region from the turbulent core region. Clearly, the enstrophy production, diffusion and dissipation are all still slowly evolving (increasing) outside the TNTI layer because the enstrophy is still adjusting to large-scale inhomogeneities within the flow. Similar conditional enstrophy budgets have been observed in TNTIs from very different flow types such as mixing layers (Watanabe *et al.* 2016*b*), plane wakes (Bisset *et al.* 2002), SFT (Holzner *et al.* 2007, 2008), boundary layers (Chauhan, Philip & Marusic 2014*a*; Borrell & Jiménez 2016; Watanabe *et al.* 2018) and plane jets (Silva & da Silva 2017; Silva *et al.* 2018; Taveira & da Silva 2014; Watanabe *et al.* 2014).

The next two figures show the conditional mean enstrophy budgets for all the simulations used in the present work, normalised by the turbulent core (figure 11*a*) and by the local (figure 11*b*) Kolmogorov velocity and length scales. It is clear that the curves in figure 11(*a*) show the same trend observed above, and do not collapse, while the curves in figure 11(*b*) not only collapse nicely into the same profiles, but are also constant for $y_I/\langle\eta\rangle_I \gtrsim 25$, i.e. shortly after the end of the TNTI layer.

In order to assess the detailed shape of each one of the conditional mean enstrophy terms obtained with the new normalisation, figure 12 shows these profiles for WAKE$_{259}$

https://doi.org/10.1017/jfm.2021.168 Published online by Cambridge University Press

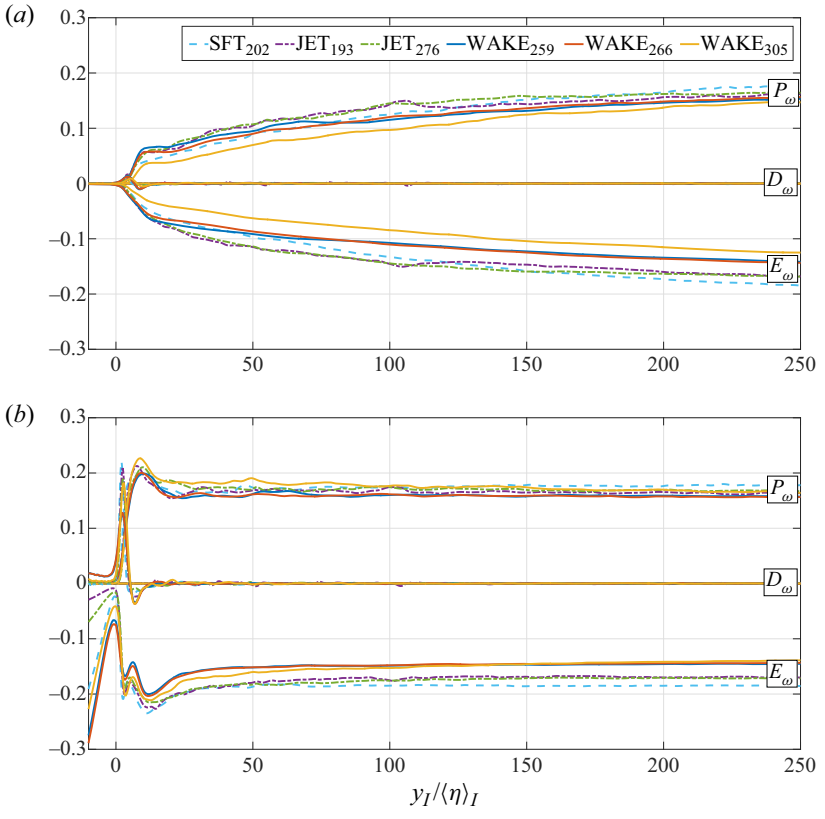

Figure 11. Normalised conditional mean profiles of the governing enstrophy equation terms (3.11) for all the simulations used in the present work, normalised with the Kolmogorov velocity and length scales, computed at the turbulent core region of the flow, $\langle\eta\rangle_T$ and $\langle u_\eta\rangle_T$ (*a*), and with the local Kolmogorov velocity and length scale, computed at the turbulent core region of the flow, $\langle\eta\rangle_I$ and $\langle u_\eta\rangle_I$ (*b*): enstrophy production (P_ω), enstrophy diffusion (D_ω) and enstrophy dissipation (E_ω).

near the TNTI layer. The evolution of enstrophy dynamics can be qualitatively interpreted in a similar manner as before with an initial part where enstrophy viscous diffusion is the leading term (VSL), followed by a region where enstrophy production takes over (TSL), until, moving further into the turbulent core, the viscous diffusion becomes negligible and production balances dissipation (turbulent core). Figure 12 also indicates the location of the VSL and TSL within the TNTI layer, and it is instructive to compare this figure with figure 10 that shows the same profiles with the standard normalisation. In short, incipient peaks of several quantities in the classical normalisation (figure 10) become much more clearly observed in the new normalisation (figure 12), which allows for a much more clear identification of the two sublayers within the TNTI layer.

In order to detect the end of the TSL (and of the TNTI layer) Silva *et al.* (2018) used a procedure based on the local maximum enstrophy, while Watanabe, Riley & Nagata (2017*c*) developed a method based on the derivative of $\langle|\omega|\rangle_I$, in respect to the distance from the IB, where the end of the TNTI layer is defined by $d\langle|\omega|\rangle_I/dy_I = 0.25\mathrm{Max}(d\langle|\omega|\rangle_I/dy_I$, with the two methods giving similar results. Figure 12 shows that using the new normalisation with the mean local Kolmogorov scales, this point simply coincides with the mean (normalised) enstrophy peak, which is located at $y_I/\langle\eta\rangle_I \approx 13$. The new normalisation thus allows for a much easier

https://doi.org/10.1017/jfm.2021.168 Published online by Cambridge University Press

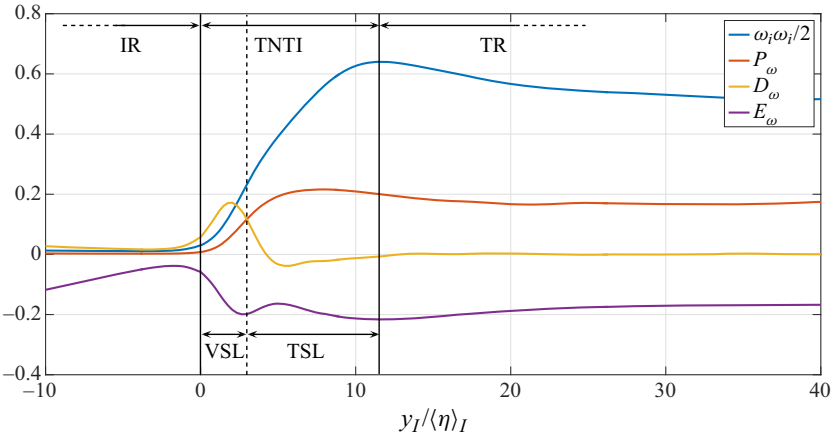

Figure 12. Conditional mean enstrophy budgets (3.11) for WAKE_{259}, normalised with the local Kolmogorov velocity and length scale, computed at the turbulent core region of the flow, $\langle\eta\rangle_I$ and $\langle u_\eta\rangle_I$, respectively: enstrophy production (P_ω), enstrophy diffusion (D_ω) and enstrophy dissipation (E_ω). The figure also displays the location of the VSL and the TSL, which comprise the TNTI layer, separating the NT (or IR) and the turbulent core (TR) regions.

	$Max[P_\omega]$	$Max[D_\omega]$	$Min[D_\omega]$	$Loc.Min[E_\omega]$	$Loc.Max[E_\omega]$	$Min[E_\omega]$
SFT_{202}	0.20(8.3)	0.22(2.0)	−0.025(6.5)	−0.21(2.7)	−0.18(4.5)	−0.24(12.6)
JET_{193}	0.21(7.6)	0.21(2.4)	−0.024(7.1)	−0.20(3.2)	−0.18(5.0)	−0.23(14.5)
JET_{276}	0.21(9.8)	0.19(2.7)	−0.013(9.0)	−0.19(3.2)	−0.17(5.0)	−0.22(12.3)
WAKE_{259}	0.22(8.0)	0.17(2.0)	−0.038(5.4)	−0.20(2.7)	−0.16(5.1)	−0.22(12.1)
WAKE_{266}	0.22(9.3)	0.16(2.0)	−0.036(6.1)	−0.19(3.0)	−0.16(5.3)	−0.21(12.1)
WAKE_{305}	0.24(12.3)	0.20(2.6)	−0.031(6.3)	−0.20(3.5)	−0.16(5.9)	−0.21(11.4)

Table 3. Details of the values and coordinates at several key points of the locally normalised enstrophy equation terms (3.11) in all the simulations used in the present work: enstrophy production (P_ω), enstrophy diffusion (D_ω) and enstrophy dissipation (E_ω). The terms are normalised with the local conditional mean Kolmogorov velocity and length scales, $\langle u_\eta\rangle_I$ and $\langle\eta\rangle_I$, respectively (e.g. $\langle P_\omega\rangle_I/(\langle u_\eta\rangle_I/\langle\eta\rangle_I)^3$), while the corresponding coordinates (indicated inside brackets) are normalised by the local mean Kolmogorov micro-scale, $y_I/\langle\eta\rangle_I$.

detection of this point and also a more direct estimation of the size of the TNTI layer. Table 3 lists the values and coordinates of the enstrophy governing terms at several key points in the new (local) normalisation, showing a small variation for these quantities for all the simulations used in the present work.

As in the 'classical' normalisation the peak of enstrophy production (P_ω) also appears during the fast increase of $\langle|\omega|\rangle_I$ in the TSL ($y_I/\langle\eta\rangle_I \approx 8.0$), however, in contrast to figure 10, in figure 12 the enstrophy production (P_ω) quickly attains a constant value once the turbulent core region is reached. The magnitude of the normalised production in the turbulent core region $\langle P^*_\omega\rangle_I = \langle P_\omega\rangle_I/\langle(u_\eta/\eta)^3\rangle_I$, which by inspection of figure 12 is $\langle P^*_\omega\rangle_I \approx 0.17$, can again be easily explained by the isotropic relations mentioned above, by remarking that normalising with (u_η/η) is equivalent to normalising with the Kolmogorov time scale $\tau_\eta = (\nu/\varepsilon)^{1/2}$, which is equal to $\tau_\eta = 1/\langle\omega_i\omega_i\rangle_I^{1/2}$ using the homogeneous flow relation $\langle 2S_{ij}S_{ij}\rangle = \langle\omega_i\omega_i\rangle$. Therefore, $\langle P^*_\omega\rangle_I = \langle P_\omega\rangle_I\langle\tau_\eta^3\rangle_I = \langle P_\omega\rangle_I/\langle\omega_i\omega_i\rangle_I^{3/2}$, which by using (3.9) with a constant value of $S_0 = -0.55$ yields $\langle P^*_\omega\rangle_I = 0.166$.

https://doi.org/10.1017/jfm.2021.168 Published online by Cambridge University Press

The enstrophy diffusion D_ω exhibits a profile which is similar in both normalisations (compare figures 10 and 12), however, in figure 12 the maximum of D_ω and P_ω is now comparable, and the maximum of D_ω is attained a bit sooner, by $y_I/\langle\eta\rangle_I \approx 2.0$. The crossing between the enstrophy production and diffusion ($D_\omega = P_\omega$), which marks the end of the VSL, is located at $y_I/\langle\eta\rangle_I \approx 4.0$ in both cases, consistently with the direct measurements of this layer undertaken by Taveira & da Silva (2014), with the smaller value obtained for the local normalisation ($y_I/\langle\eta\rangle_T = 4.2$ and $y_I/\langle\eta\rangle_I = 3.1$).

The enstrophy dissipation term (E_ω) is the only term that displays a very different shape compared with the usual normalised profile (compare E_ω in figures 10 and 12). The profile also displays a constant value once the end of the TNTI layer is approached, roughly coinciding with a second minimum at $y_I/\langle\eta\rangle_I \approx 12.1$, however, the profile also exhibits another minimum very close to the IB, at $y_I/\langle\eta\rangle_I \approx 2.7$, coinciding with the end of the VSL, and a local maximum within the TSL at $y_I/\langle\eta\rangle_I \approx 5.1$, i.e. slightly before (but very close to) the point of maximum enstrophy production and minimum of enstrophy diffusion. This local maximum in E_ω roughly coincides with the minimum of enstrophy diffusion D_ω and indicates that these two viscous effects are interrelated. The JPDF between these two variables shows indeed a very strong (anti)correlation between the two variables at this location (not shown).

To summarise, the new normalisation of the enstrophy transport equation terms using the local mean Kolmogorov velocity and length scales shows that the conditional mean profiles of these terms exhibit a universal shape, with very small variations in the simulations used in the present work, and allows for a much more clear assessment of the position of the several sublayers within the TNTI layer, as well as the limits of this layer.

This fact has an important implication on the statistics of the small-scale 'nibbling' mechanism as measured in different flow types. The 'nibbling' mechanism, as defined by Corrsin & Kistler (1955), consists of the small-scale diffusion of vorticity (or enstrophy) into the NT flow region, which occurs mainly at the VSL, where the enstrophy diffusion D_ω dominates the enstrophy dynamics. The total amount of this effect can be computed in several different ways, e.g. by computing a 'flux' of D_ω across the edge of the VSL, or by integrating D_ω over the entire VSL. Whatever the definition used, the fact that the mean profile of D_ω, normalised with the local mean Kolmogorov velocity and length scales, is equal in very different flow types strongly suggests that the statistics of the 'nibbling' mechanism are universal, i.e. equal in jets, wakes and mixing layers.

The next section will show how the instantaneous values associated with the small-scale turbulence dynamics, as observed by the shape of the probability density functions, also collapse nicely into the same contours, provided these quantities are properly normalised.

3.3. *Probability density functions at several locations within the TNTI layer*

In order to assess the degree of collapse provided by the new normalisation we now analyse joint probability density functions (JPDFs) of several quantities at fixed coordinates within the TNTI layer. These JPDFs were computed by using the values of several flow variables taken at the same (fixed) distance y_I from the IB position, using the same procedure described in § 2.2. Thus, the approach used to obtain these JPDFs is quite different to that developed in Pope (1985), which to the authors knowledge has never been used in the context of TNTIs. Figure 13 shows the JPDF of the total enstrophy variation T_ω and enstrophy viscous diffusion D_ω at four locations inside the TNTI layer. The two variables are again normalised with the local, i.e. conditional mean Kolmogorov velocity

https://doi.org/10.1017/jfm.2021.168 Published online by Cambridge University Press

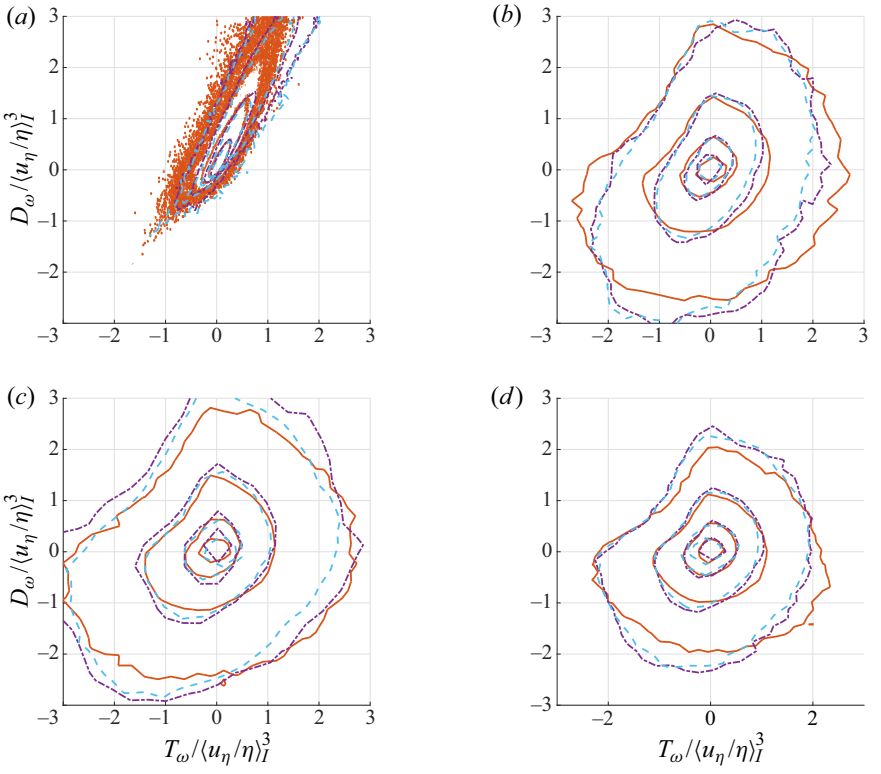

Figure 13. Joint probability density function of total enstrophy variation T_ω, and enstrophy diffusion, D_ω, normalised with the (mean) local Kolmogorov velocity and length scale, for three different flow types (SFT_{202} – dash/blue, JET_{193} – dash–dot/magenta, $WAKE_{266}$ – solid line/red) at several locations within the TNTI layer: (*a*) peak of enstrophy diffusion $Max[D_\omega]$; (*b*) peak of enstrophy production $Max[P_\omega]$; (*c*) peak of enstrophy $Max[\omega^2/2]$; (*d*) turbulent core region ($y_I/\langle\eta\rangle_I = 250$). In all cases the isolines correspond to the same levels (1.0, 0.1, 0.01 and 0.001).

and micro-scale. In agreement with Taveira *et al.* (2013), the correlation between T_ω and D_ω is very strong inside the VSL at the point of maximum D_ω (figure 13*a*) and decreases inside the TSL and beyond (figure 13*b–d*). The universality of the enstrophy dynamics within the TNTI layer can be confirmed by the strong near collapse of the isolines of the JPDFs for three very different flow types, particularly for the contours associated with the most frequent values of the variables. The smaller degree of collapse observed for high values of T_ω and D_ω in the first location (figure 13*a*) can be explained by the very fast evolution of the small-scale characteristics at this point of $Max[D_\omega]$, and the smaller collapse between the curves for the contours associated with less frequent events may also be affected by the use of the interface envelope, instead of the interface itself, in the procedure of the conditional statistics used in the present work.

Figure 14 shows the JPDF of the total enstrophy variation T_ω and enstrophy production P_ω at the same four locations of the TNTI layer as in figure 13. Again, and in agreement with Taveira *et al.* (2013), we see that the correlation between T_ω and P_ω is strong in the entire TSL and in the turbulent core region (figure 13*b–d*) but is somehow much smaller inside the VSL (figure 14*a*). Again the collapse between the isolines of the JPDF of T_ω and P_ω is very impressive, particularly for the contours associated with the most

https://doi.org/10.1017/jfm.2021.168 Published online by Cambridge University Press

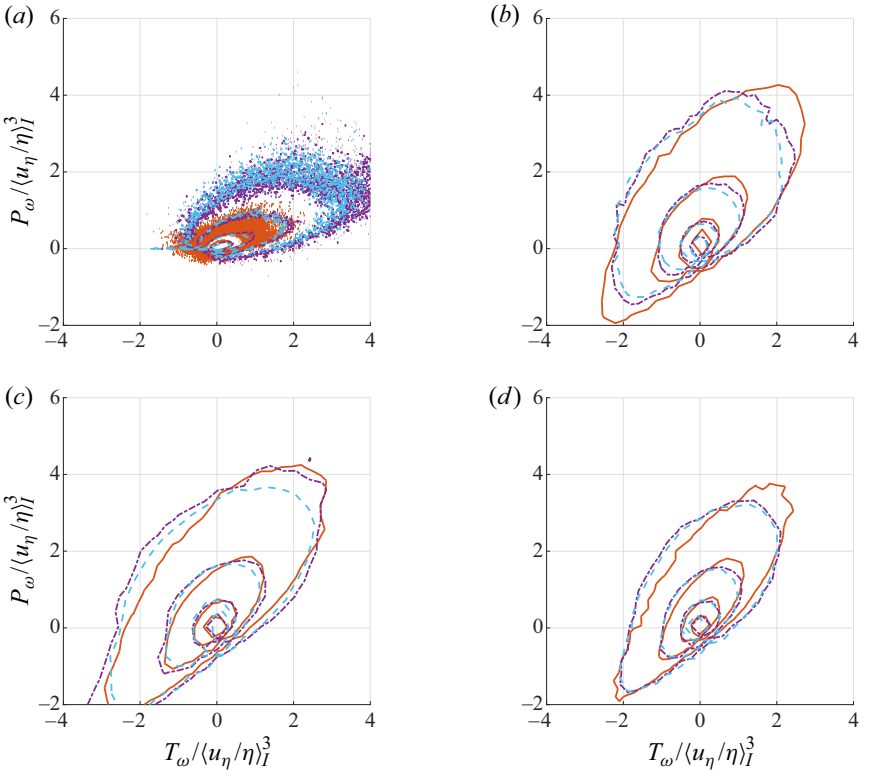

Figure 14. Joint probability density function of total enstrophy variation T_ω, and enstrophy production, P_ω, normalised with the (mean) local Kolmogorov velocity and length scale, for three different flow types (SFT_{202} – dash/blue, JET_{193} – dash–dot/magenta, $WAKE_{266}$ – solid line/red) at several locations within the TNTI layer: (*a*) peak of enstrophy diffusion $Max[D_\omega]$; (*b*) peak of enstrophy production $Max[P_\omega]$; (*c*) peak of enstrophy $Max[\omega^2/2]$; (*d*) turbulent core region ($y_I/\langle\eta\rangle_I = 250$). In all cases the isolines correspond to the same levels (1.0, 0.1, 0.01 and 0.001).

frequent values, and the fact that these are obtained from very different flows underscores the universality of the enstrophy dynamics within the TNTI layer.

The evolution of small scales of turbulence inside the TNTI layer is further explored by analysing the JPDFs for the second Q, and third R, invariants of the velocity gradient tensor, $\partial u_i/\partial x_j$. The invariants are interesting variables to analyse in this context because they characterise many of the well-know universal features of the small-scale dynamics of turbulence, including the geometry of the small-scale straining motions as well as the small-scale details of the strain and vorticity generation (Cantwell 1993; Davidson 2004). This universality is manifested in the well-know 'tear-drop' shape of the JPDF of Q and R that has been observed in virtually all turbulent flows, such as in experimental turbulent boundary layers (Elsinga & Marusic 2010), round jets (Breda & Buxton 2019) and turbulence generated by fractal grids (Gomes-Fernandes, Ganapathisubramani & Vassilicos 2014), and in numerical simulations of turbulent mixing layers (Soria *et al.* 1994), turbulent channel flows (Blackburn, Mansour & Cantwell 1996), turbulent boundary layers (Chong *et al.* 1998), forced and decaying isotropic turbulence (Ooi *et al.* 1999), shear-free turbulence (Watanabe *et al.* 2017*a*) and turbulent plane jets (da Silva & Pereira 2008).

https://doi.org/10.1017/jfm.2021.168 Published online by Cambridge University Press

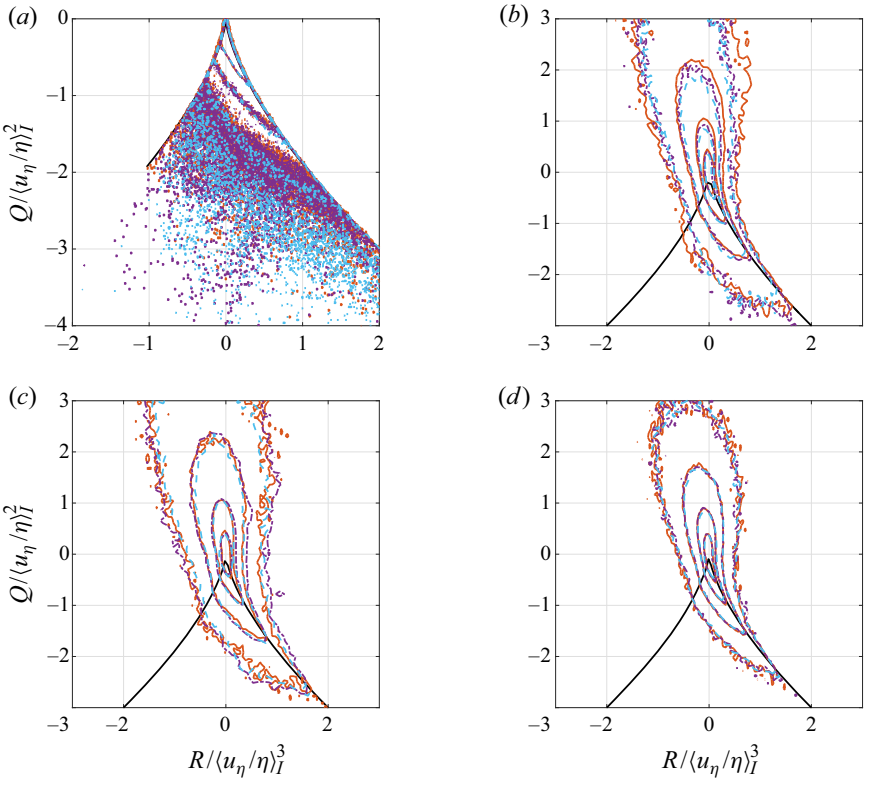

Figure 15. Joint probability density function of the second Q and third R invariants of the velocity gradient tensor, normalised with the (mean) local Kolmogorov velocity and length scale, for three different flow types (SFT_{202} – dash/blue, JET_{193} – dash–dot/magenta, $WAKE_{266}$ – solid line/red) at several locations within the TNTI layer: (*a*) IB ($y_I/\langle\eta\rangle_I$); (*b*) peak of enstrophy production $Max[P_\omega]$; (*c*) peak of enstrophy $Max[\omega^2/2]$; (*d*) turbulent core region ($y_I/\langle\eta\rangle_I = 250$). In all cases the isolines correspond to the same levels (1.0, 0.1, 0.01 and 0.001). The lines represent the zero discriminant $4Q^3 + 27R^2 = 0$ (Cantwell 1993; Davidson 2004) (note that the line is actually plotted for each case but are indistinguishable due to the collapsing).

However, the so-called 'tear-drop' shape is not completely formed in the IR (or NT) region and the build-up of this shape across the TNTI layer has been analysed in detail by da Silva & Pereira (2008) and, more recently, by Watanabe *et al.* (2017*a*). Figure 15 shows the evolution of the JPDF of Q and R from the IB to the turbulent core region for the three different flow configurations analysed in figures 13 and 14. The invariants are again normalised using the local (conditional mean) Kolmogorov velocity and length scales. As in da Silva & Pereira (2008), Watanabe *et al.* (2017*a*), the tear-drop starts forming in the fourth quadrant, inside the VSL (figure 15*a*), and expands later in the second quadrant when crossing the TSL (figure 15*b*), and is completely formed and virtually equal to deep inside the turbulent region by the time the end of the TNTI layer is reached (figure 15*c*,*d*). Recall that using the classical 'normalisation' differences in these maps can be observed while moving away from the IB (for the same flow), e.g. da Silva & Pereira (2008), and this is clearly not the case here. On the contrary, the almost perfect collapse observed for these JPDFs at three radically different flow configurations, and at different locations, even for the most frequent events, again demonstrates the universality of the small-scale geometry, and of the dynamics of strain and vorticity within the TNTI layer.

https://doi.org/10.1017/jfm.2021.168 Published online by Cambridge University Press

4. Conclusions

The universality of the statistics of the small-scale motions is the cornerstone of the theory of turbulence and can take many different forms in fully developed turbulence (Davidson 2004). The goal of the present work is to investigate the evidence of a similar universality in the small-scale statistics near the TNTI layer that exists at the edges of many flows such as turbulent jets, wakes and mixing layers, and also in turbulent boundary layers. The small-scale variables analysed here are the basic variables typically considered when assessing the small scales of motion in turbulent flows: vorticity and strain (and related quantities).

For this purpose, we carried out DNS of three different temporally evolving free shear flows: JET, WAKE and SFT (i.e. a turbulent front evolving without mean shear (SFT). The DNS of JET and SFT have been documented before, and the new DNS of WAKE have been validated against available data from experiments and DNS. In all the data banks the resolution is comparable to the Kolmogorov micro-scale, and the Reynolds number (based in the Taylor scale) is greater than $\langle Re_\lambda \rangle_I \gtrsim 200$, which is required to obtain the asymptotic solutions of the TNTI dynamics (Silva *et al.* 2018).

A series of conditional mean profiles were obtained as a function of the distance from the IB, which marks the outer surface of the TNTI layer. These profiles showed that the Kolmogorov velocity and length scale are approximately constant, and equal to the values deep inside the turbulent core of the flow for the entirety of the TNTI layer, changing only close to the IB, at the VSL region, i.e. for distances of less than $\approx 5\eta$ from the IB position.

For all the flow types and Reynolds numbers analysed in the present work, the conditional mean enstrophy profiles normalised by the turbulent core Kolmogorov velocity and length scales exhibit a sharp entrophy jump near the IB, followed by a slower increase moving into the turbulent core region, with different profiles for the different cases. In contrast, the normalisation of the same quantity using the local Kolmogorov velocity and length scales shows that all the mean enstrophy profiles collapse into a single curve. The peculiar 'bump' observed in these profiles at a distance of $\approx 10\eta$ from the IB, representing a deviation of the flow from a state of local homogeneity in that region, can be explained by the existence of regions of low pressure caused by a row of intense (tube-like) vorticity structures, with axis aligned with tangent to the isosurface defining the IB. The skewness of the longitudinal velocity gradient also confirms that the smallest scales of motion exhibit approximately local isotropic statistics except very close to the IB position (for distances from the IB smaller than $\approx 10\eta$).

Other small-scale quantities such as the second invariant of the velocity gradient tensor and strain magnitude, and of the individual terms governing the evolution of the enstrophy inside the TNTI layer, also collapse into single mean profiles when normalised by the local Kolmogorov velocity and length scales. These mean profiles also allow for a better identification of the VSL and the TSL within the TNTI layer, because of clearly identifiable maxima and minima in the mean profiles of the enstrophy governing terms. Finally, the JPDFs of the total enstrophy variation, viscous diffusion and production, together with the second and third invariants of the velocity gradient tensor, show an approximate collapse of the statistics of instantaneous values of these variables in the three flow types and at the same positions inside the TNTI layer when these are normalised by the local Kolmogorov velocity and length scales. The results confirm that the statistics of the small scales of motion within the TNTI layer are universal, i.e. are equal for different flow types at different Reynolds numbers, provided the Reynolds number is sufficiently high, and suggest that the statistics of the small-scale 'nibbling' mechanism, associated with the mechanism of the TE, is universal.

https://doi.org/10.1017/jfm.2021.168 Published online by Cambridge University Press

Acknowledgements. We acknowledge PRACE for awarding us access to resource Marenostrum IV based in Spain at https://www.bsc.es. The authors further acknowledge the Laboratory for Advanced Computing at the University of Coimbra for providing HPC, computing and consulting resources (http://www.lca.uc.pt). The authors acknowledge Minho Advanced Computing Center for providing HPC computing and consulting resources that have contributed to the research results reported within this paper (https://macc.fccn.pt).

Funding. C.B. da Silva acknowledges Fundação para a Ciência e a Tecnologia (FCT) through IDMEC, under LAETA, projects UIDB/50022/2020, and through project PTDC/EMS-ENE/6129/2014, and M. Zecchetto acknowledges Fundação para a Ciência e a Tecnologia (FCT) for SFRH/BD/144291/2019.

Declaration of interests. The authors report no conflict of interest.

Author ORCIDs.
Marco Zecchetto https://orcid.org/0000-0002-7506-2631;
Carlos B. da Silva https://orcid.org/0000-0002-6866-5469.

Appendix A. Assessment of the new DNS of WAKE

The transition scenario is similar in all the new DNS of temporal planar wakes. It typically starts by the emergence of symmetrical pairs of spanwise large-scale rollers at the upper and lower shear layer region, and is followed by the appearance of pairs of streamwise vortices connecting each two consecutive pairs of the rollers, making up the classical Von Kármán street. Shortly after, the streamwise vortices break up into smaller-scale structures, with no clear preferential direction, which is a sign of the flow having attained a fully developed turbulent stage.

An interesting feature well known to wakes is that, in contrast to jets, very different outlines of the shear layer can be observed in different wakes. This is illustrated in figure 16 which shows the contours of vorticity magnitude from two of the new planar wake simulations, WAKE_{259} and WAKE_{266}. Whereas the shear layer is generally extended along the streamwise direction in WAKE_{259}, it is much more 'twisted' in WAKE_{266}. Moser, Rogers & Ewing (1998) also observed that different initial conditions could originate wakes in the fully developed turbulent region, with dramatically different pictures, although with somehow not too different classical statistics. The difference between jets and wakes in this respect may be connected with the way jets/wakes 'forget'/'do not forget' the particular initial or inlet velocity characteristics during the transition to turbulence. Figures 17(a) and 17(b) show the temporal evolution of the centreline velocity deficit $U_s(t) = U_\infty - \langle u(y = 0, t)\rangle$, where U_∞ is the free stream velocity, and of the wake half-width $\delta_{05}(t)$, for the three wakes used in the present work, respectively. The brackets ($\langle\rangle = \langle\rangle_{x,z}$) represents a (spatial) average in the streamwise (x) and spanwise (z) directions (the centreline of the wake is at $y = 0$). As described in Moser *et al.* (1998), these variables should evolve as

$$U_s(t) \sim (t - t_0)^{-1/2} \tag{A1}$$

and

$$\delta_{05}(t) \sim (t - t_0)^{1/2}, \tag{A2}$$

respectively, where t_0 is a 'virtual' time origin. Only a few instants are available for the computation of these quantities in the simulated wakes reported here, but figures 17(a) and 17(b) show that $\delta_{05}^2(t)$ and $1/U_s(t)^2$ display an approximately linear evolution with time, although with different slopes, which agrees with the temporal wakes simulated in Moser *et al.* (1998) and indicates that at the instants considered the three wakes are evolving as in the self-similar in the equilibrium region.

https://doi.org/10.1017/jfm.2021.168 Published online by Cambridge University Press

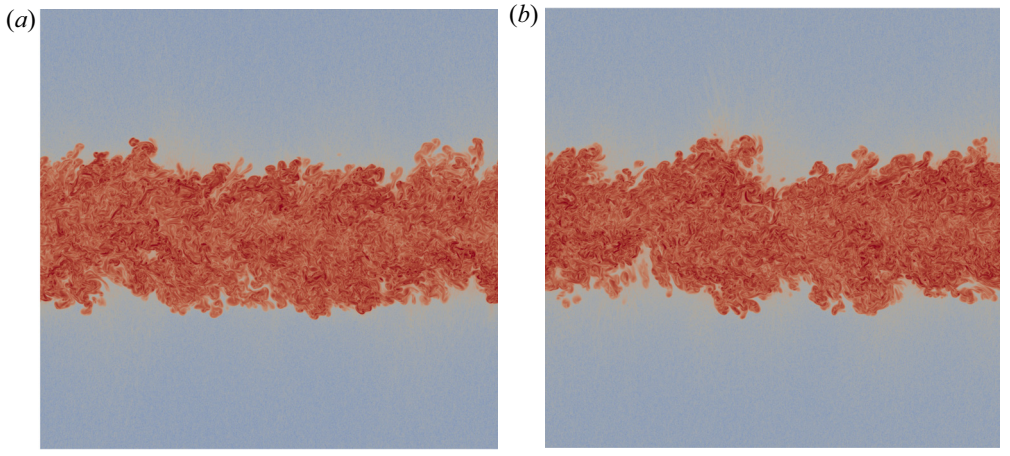

Figure 16. Contours of vorticity magnitude in a (x, y) plane for two DNS of planar wakes: WAKE_{259} and WAKE_{266}, at the fully developed turbulent regime. The figures show the total extent of the computational domain in the streamwise (x) and normal (y) directions. (a) WAKE_{259} and (b) WAKE_{266}.

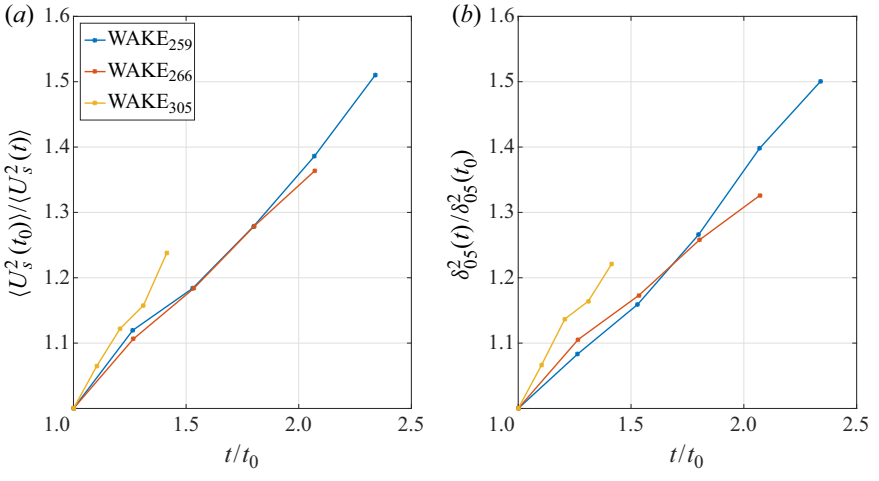

Figure 17. Temporal evolution of the mean velocity deficit U_s (a) and half-width δ_{05} (b) for the three wakes considered in this study. Only a few instants marked (by the symbols) are available for these plots (t_0 is a 'virtual' initial time).

Since the temporally evolving plane wake is statistically homogeneous in the streamwise and spanwise directions, the streamwise momentum equation can be used to derive the equation governing the mean velocity deficit $\Delta U(y, t)$,

$$\frac{\partial \Delta U}{\partial t} = \frac{\partial \langle u'v' \rangle}{\partial y} + \nu \frac{\partial^2 \Delta U}{\partial y^2}, \tag{A3}$$

where $\Delta U(y, t) = U_\infty - \langle u(y, t) \rangle$ is the profile of the mean velocity deficit and $u'(x, y, z, t)$ and $v'(x, y, z, t)$ are the velocity fluctuations in the streamwise and normal directions, respectively, i.e. the instantaneous velocity is $u(x, y, z, t) = \langle u(y, t) \rangle + u'(x, y, z, t)$ according to the Reynolds decomposition.

https://doi.org/10.1017/jfm.2021.168 Published online by Cambridge University Press

The classical theory for the far field of fully developed turbulent shear flows establishes the existence of a self-similar state, which is reached when all the properly normalised turbulence statistics attain universal distributions that are independent of streamwise location (Townsend 1976). This assumption relies on the idea that during the transition to turbulence the different initial details (inlet conditions) from different wakes are lost, so that a universal asymptotic self-similar condition is attained.

For the particular case of planar turbulent wakes, similarity solutions for the velocity deficit and shear stresses are given by (Townsend 1976; George 1989; Moser *et al.* 1998),

$$\Delta U(y,t) = -U_s(t) f(\xi) \tag{A4}$$

and

$$\langle u'v'(y,t)\rangle = R_s(t) g(\xi), \tag{A5}$$

where $\xi = y/\delta_{05}(t)$ is a similarity coordinate defined with the half-width of the wake and $f(\xi)$ the normalised velocity defect profile. Similarly, the normalised Reynolds stresses $g(\xi)$ are defined with the help of a normalisation function $R_s(t)$, usually taken as $R_s(t) = U_s^2(t)$.

By neglecting the viscous term in (A3) and by assuming a constant turbulent viscosity, one arrives at the self-similar velocity defect profile (e.g. Pope 2000),

$$f(\xi) = exp(-\alpha\xi^2), \tag{A6}$$

with $\alpha = \ln(2) \approx 0.693$. Wygnanski, Champagne & Marasli (1986) carried out experiments in two-dimensional small-deficit wakes using various wake generators, including circular cylinders, a symmetrical airfoil, a flat plate and an assortment of screens of varying solidity. They showed that using the similarity coordinates the (normalised) mean velocity profiles of all the wake generators collapsed into a single curve described by the function

$$f(\xi) = exp(-0.637\xi^2 - 0.056\xi^4), \tag{A7}$$

where the fourth-order term was added to correct the overestimate of (A6) observed near the wake edges. Moser *et al.* (1998) carried out DNS of temporal planar wakes using as an initial condition three different realisations of previously simulated turbulent boundary layers. The boundary layers only differ in the magnitude of the initial perturbations, and originate three very distinct wakes (unforced, weakly forced, strongly forced).

Figure 18 shows the normalised velocity defect profile $f(\xi)$ from the present wake simulations (at the far field regime) compared with the experimental data obtained by Wygnanski *et al.* (1986) and by Ramaprian *et al.* (1984), and two of the available DNS profiles generated by Moser *et al.* (1998). The figure also shows the functions described by (A6) and (A7). The degree of convergence of the numerical results is not perfect and is typical of similar results obtained in other temporal numerical simulations, where the averaging procedure is carried out using a single instantaneous field (e.g. Rogers & Moser 1994). However, all the profiles, including the present wake simulations, exhibit a good collapse into the same curve. The slight deviation of the profile maximum of the simulation WAKE_{305} from $y/\delta_{0.5} = 0$ is caused by the asymmetry of the large-scale motions at the instant used for the analysis.

Figure 19 shows the profiles of the normal Reynolds stresses in the streamwise direction, from several experimental and numerical results, compared with the profiles from present wake simulations. The scatter between the several curves is substantial, unlike with the mean velocity deficit. This is a well-known consequence of the strong dependence of the turbulent wake characteristics from the details of the initial conditions. Indeed, it has

https://doi.org/10.1017/jfm.2021.168 Published online by Cambridge University Press

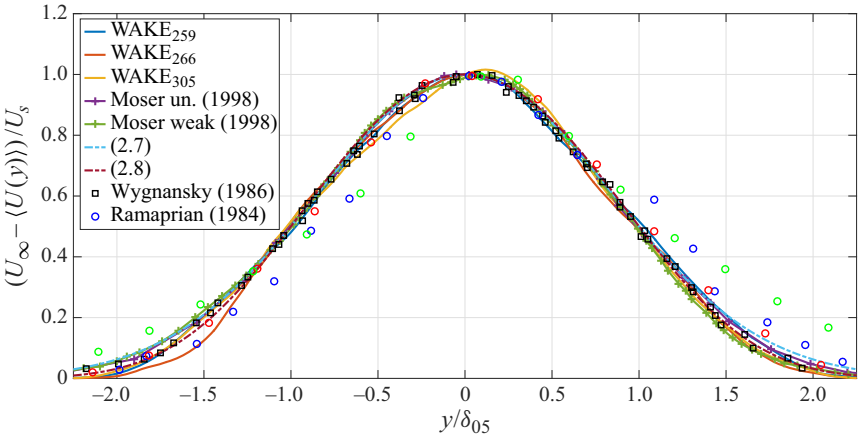

Figure 18. Normalised velocity defect profiles from several experimental and numerical results, compared with the present wake simulations: (solid lines) wakes in table 1; (solid lines with symbols) unforced wake and weakly forced wake obtained by DNS in Moser *et al.* (1998); (dash–dotted line) constant turbulent viscosity solution, (A6) in Pope (2000); (dashed line) (A7) from Wygnanski *et al.* (1986); (□) experimental data from Wygnanski *et al.* (1986); (○) experimental data from Ramaprian *et al.* (1984).

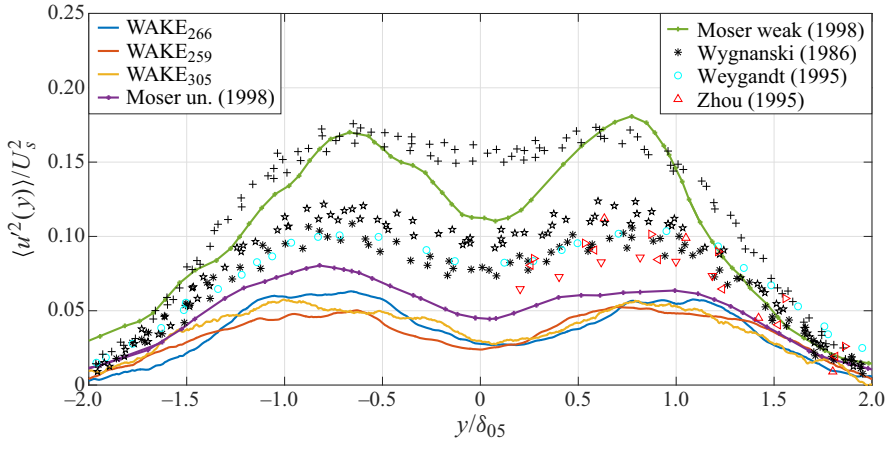

Figure 19. Normalised longitudinal component of the Reynolds stresses from several experimental and numerical results, compared with the present wake simulations: (solid lines) wakes in table 1; (solid lines with symbols) unforced wake and weakly forced wake obtained by DNS in Moser *et al.* (1998); (dark symbols) experimental data from Wygnanski *et al.* (1986); (○) experimental data from Weygandt & Mehta (1995); (red triangles) experimental data from Zhou & Antonia (1995).

been frequently shown that, unlike as predicted from the classical theory, the Reynolds stresses from wakes originated from different generators do not collapse into the same scaling curve (Wygnanski *et al.* 1986; Weygandt & Mehta 1995; Zhou & Antonia 1995). Nevertheless, the agreement between the several profiles is reasonable, since all Reynolds stresses profiles exhibit a similar double-peaked shape, with a maximum of roughly $\langle u^2\rangle/U_s^2 \approx 0.05 - 0.06$. The other Reynolds stresses components (not shown) display a similar agreement. Thus, the large scales of the flow are characteristic of the far field of WAKE.

https://doi.org/10.1017/jfm.2021.168 Published online by Cambridge University Press

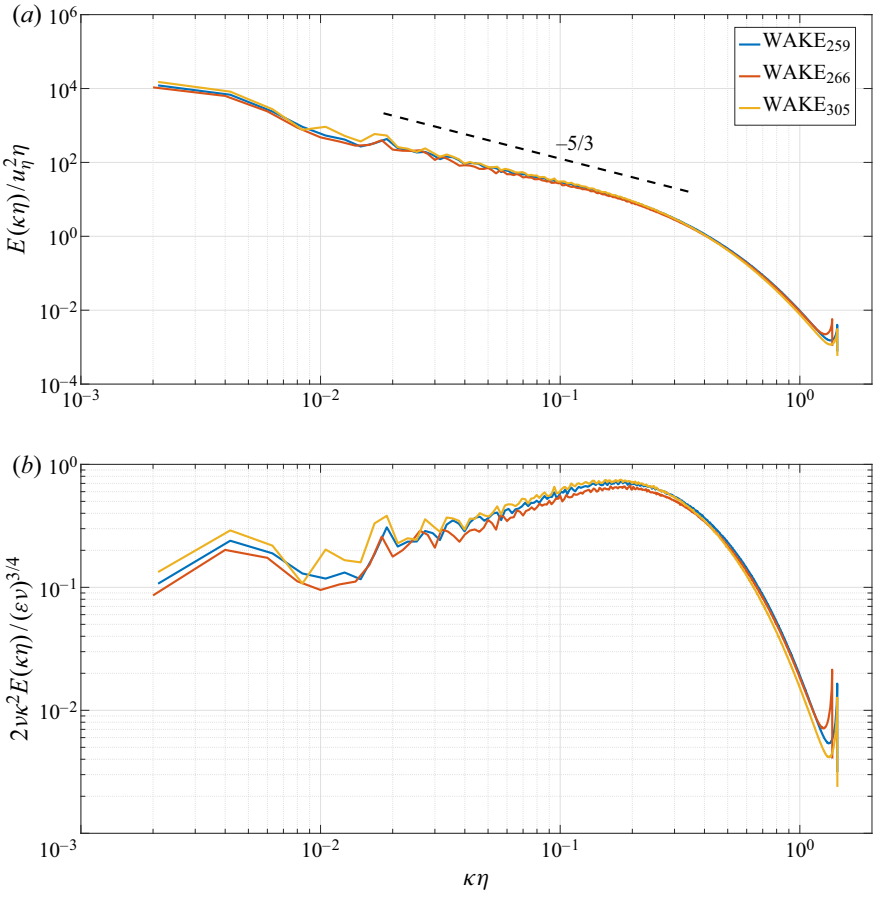

Figure 20. Three-dimensional kinetic energy spectra (*a*) and enstrophy spectra (*b*) for the simulations WAKE_{259}, WAKE_{266} and WAKE_{305}. The spectra are normalised with the Kolmogorov quantities and are computed using the entire flow domain.

The resolution of the small scales of motion in the new planar wakes simulations can be appreciated in figures 20(*a*) and 20(*b*), which show the 3-D kinetic energy spectra, and enstrophy spectra, for all the simulations. In all cases the kinetic energy spectrum displays a reasonable $-5/3$ inertial range region, followed by a smooth decay at high wavenumbers, and the resolution is always above $\kappa_{max}\eta \approx 1.3$. All the enstrophy spectra peak at $k\eta \approx 0.13$, which marks the start of the dissipation region (Donzis & Sreenivasan 2010) and are also followed by a smooth decay at high wavenumbers. Thus, the small scales of motion are well resolved for all the simulations which completes the validation of the new temporal wake simulations.

Appendix B. Analytical description of the profiles of conditional mean enstrophy

The shape of the profiles of conditional mean enstrophy, normalised by the reference Kolmogorov velocity and length scale from the turbulent core region, as depicted in figure 4, can be justified by analysing the enstrophy transport (3.11). In this analysis we denote the enstrophy by $\Omega(z) = \langle\omega_i\omega_i\rangle_I/2$ and the distance from the IB normalised by the reference Kolmogorov length scale by $z = y_I/\langle\eta\rangle_T$. By supposing that the total enstrophy

https://doi.org/10.1017/jfm.2021.168 Published online by Cambridge University Press

variation T_ω occurs at a much smaller time scale than the sum of the other terms, which is well supported by the present data and virtually all existing data of similar enstrophy budgets, we can write (3.11) as

$$P_\omega + D_\omega - E_\omega \approx 0. \tag{B1}$$

In the initial part of the VSL region, when the production is still inactive, the diffusion and dissipation roughly balance, so that (B1) can be written as

$$D_\omega - E_\omega \approx 0. \tag{B2}$$

The enstrophy diffusion is composed of many terms but, arguably, at the start of the VSL region the leading order term involves the second derivative of the enstrophy in relation to the normal of the IB position,

$$D_\omega = \left\langle \nu \frac{\partial^2(\omega_i\omega_i/2)}{\partial x_j \partial x_j} \right\rangle_I \approx \nu B \frac{\mathrm{d}^2\Omega(z)}{\mathrm{d}z^2}, \tag{B3}$$

where B is a constant of order $O(1)$. On the other hand, the dissipation term can be approximated by considering that each one of the vorticity derivatives involved in its definition can be approximated considering local isotropic turbulence, i.e. $\partial\omega_i/\partial x_j \sim \omega_i/\langle\eta\rangle_T$, so that

$$E_\omega = \langle \nu \nabla\omega_i \cdot \nabla\omega_i \rangle_I \approx \nu C \frac{\Omega(z)}{\langle\eta_T\rangle^2}, \tag{B4}$$

where C is a constant of order one. Thus, the conditional mean enstrophy is the solution of the equation

$$\frac{\mathrm{d}^2\Omega}{\mathrm{d}z^2} - C'\Omega = 0, \tag{B5}$$

where $C' = C/B\langle\eta\rangle_T^2$, whose solution is

$$\Omega(z) = c_1 exp(+c_3 z) + c_2 exp(-c_3 z), \tag{B6}$$

with $c_3 = \sqrt{C'}$, and where c_1 and c_2 are constants. Since the enstrophy is zero at the IB, $\Omega(0) = 0$, $c_1 + c_2 = 0$. So that (B6) can be written as

$$\Omega(z) = c_1 exp(+c_3 z) - c_1 exp(-c_3 z) = 2c_1 \sinh(c_3 z). \tag{B7}$$

This solution is consistent with the initial growth of enstrophy in the first few Kolmogorov micro-scales of the VSL (before P_ω starts to rise).

Further inside the TNTI layer, in the early part of the TSL, when the production and dissipation roughly balance while diffusion is still $D_\omega \neq 0$, (B1) simplifies to

$$D_\omega \approx 0, \tag{B8}$$

and can be approximated by

$$\frac{\mathrm{d}^2\Omega}{\mathrm{d}z^2} = 0, \tag{B9}$$

whose solution is $\Omega(z) = b_1 z + b_2$, where b_1 and b_2 are constants. Thus, the conditional mean enstrophy evolves linearly with the normal direction at some subregion of the TSL.

Finally, towards the end of the TSL, the enstrophy approaches a saturation before the flow attains the turbulent core region. This maximum enstrophy (saturation) value is

https://doi.org/10.1017/jfm.2021.168 Published online by Cambridge University Press

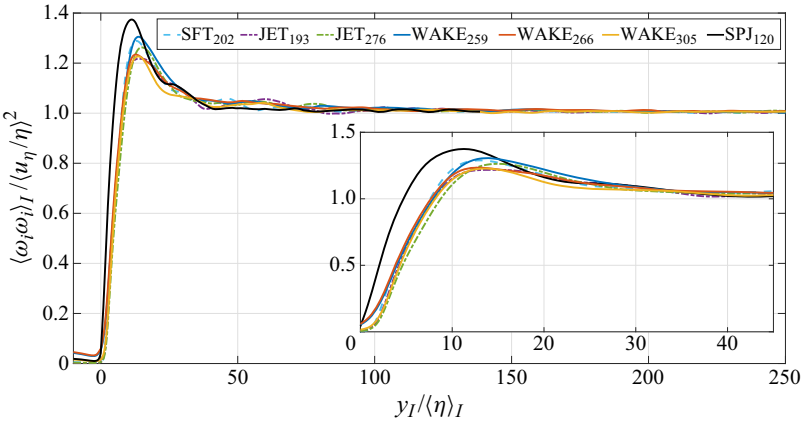

Figure 21. Conditional mean enstrophy profile $\langle\omega_i\omega_i\rangle_I$, shown in figure 5 together with the results for the DNS of a spatially evolving turbulent planar jet (SPJ_{120}). All the profiles are normalised with the local mean Kolmogorov velocity and length scale, computed at each coordinate y_I, $\langle\eta\rangle_I$ and $\langle u_\eta\rangle_I$, respectively. The inset shows the amplified region near the IB ($y_I = 0$).

naturally imposed by the large scales of the flow, since in the turbulent core region the dissipation law implies that $\Omega(z) \sim u'^3/\nu L$, where u' and L are the root-mean-square velocity and the turbulent integral scale, respectively. After this saturation region the enstrophy increases slowly moving into the flow centreline, while the production and dissipation approximately balance, $P_\omega \approx E_\omega$, while the diffusion is close to zero $D_\omega \approx 0$, which is consistent with a roughly constant conditional mean enstrophy.

Appendix C. Effects of the temporal vs spatial flow type in the conditional enstrophy profiles

In order to assess whether the spatial or temporal nature of the simulations/flow type can affect the present results we have added results from a DNS of a spatially evolving flow. In the present case a turbulent planar jet has been used. The code used for these spatial simulations has been described more recently in Guimarães *et al.* (2020). The code uses a number of $N_x \times N_y \times N_z = 1536 \times 1536 \times 256$ grid points along the streamwise, normal and spanwise directions, respectively, and the computational domain extends to $(L_x \times L_y \times L_z) = (24H \times 24H \times 4H)$ in the same directions, respectively, as in da Silva, Lopes & Raman (2015). The ratio of the inlet slot-width to the inlet momentum thickness was $H/\theta = 30$, and the inlet Reynolds number was $Re_H = 3500$. The pictures of this simulation, e.g. the contours of vorticity magnitude, are similar to those observed in JET, such as in da Silva *et al.* (2015) and, more recently, in Guimarães *et al.* (2020). The flow is in the fully developed turbulent region for $x/H \gtrsim 10$ and for the present work, a total of 50 instantaneous fields were taken from the region between $21 \leq x/H \leq 22$, where the Taylor-based Reynolds number is estimated as $Re_\lambda \approx 120$.

The conditional mean profiles of enstrophy for this flow are shown in figure 21, where the new curve is added to the results of figure 5. It is clear that the results for the spatial jet (SPJ_{120}) are similar to the curves obtained for the other simulations extensibly discussed in § 3.1, which shows that the temporal or spatial nature of the simulations does not affect the results in the present paper. The agreement would be even better had the Reynolds number for this simulation been a bit higher, as discussed in Appendix D.

https://doi.org/10.1017/jfm.2021.168 Published online by Cambridge University Press

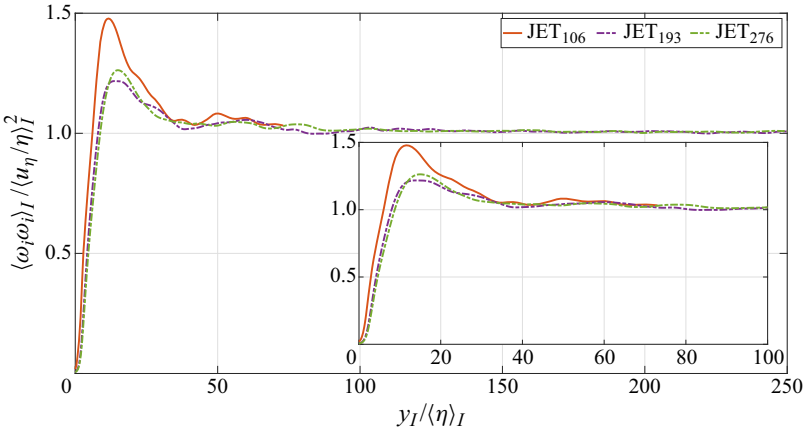

Figure 22. Conditional mean enstrophy profiles $\langle\omega_i\omega_i\rangle_I$ for three temporally evolving JET: JET_{193}, JET_{276} (already in the core of the paper) and a new case with JET_{106}. All the profiles are normalised with the local mean Kolmogorov velocity and length scale, computed at each coordinate y_I, $\langle\eta\rangle_I$ and $\langle u_\eta\rangle_I$, respectively. The inset shows the amplified region near the IB ($y_I = 0$).

Appendix D. Effects of the Reynolds number in the conditional enstrophy profiles

In order to assess the effect of the Reynolds number in the shape of the conditional mean enstrophy profiles we have compiled the results obtained from three different DNS of temporal planar jets. Two of these DNS (JET_{193} and JET_{276}) are already used in the core of the present paper and have been used in many figures. To these cases we have added a new simulation with (JET_{106}) the same planar jet configuration, but using a much lower Reynolds number. All the parameters of this simulation are equal to JET_{193} (e.g. same grid size and computational box), but the initial Reynolds number is set to $Re_H = 3000$. We use an instantaneous field taken from the far field region of this DNS where the Taylor-based Reynolds number is equal to $Re_\lambda = 106$.

The conditional mean profiles of enstrophy for the three simulations are shown in figure 22, where the new curve is added to the results of this configuration already shown in figure 5. The differences between the two curves with the highest Reynolds numbers are very small, as the collapse is only imperfect due to very small oscillations clearly connected with the imperfect convergence of the curves. However, for the smaller Reynolds number the observed peak is a bit higher, with $Max\{\langle\omega_i\omega_i\rangle_I/\langle(u_\eta/\eta)^2\rangle_I\} \approx 1.47$, compared with $Max\{\langle\omega_i\omega_i\rangle_I/\langle(u_\eta/\eta)^2\rangle_I\} \approx 1.23$ and 1.27 for JET_{193} and JET_{276}, respectively. The location of this peak is also somehow a bit close to the IB for JET_{106} with $\delta_{Max|\omega|} \approx 11.6$, compared with $\delta_{Max|\omega|} \approx 14.1$ and 14.9 for JET_{193} and JET_{276}, respectively.

Thus, the Reynolds number has a small effect (of slightly increasing the peak of the conditional enstrophy) for low Reynolds numbers that, however, ceases to be observed for sufficiently high Reynolds numbers. This result is not surprising since a threshold of $Re_\lambda \gtrsim 200$ has been shown to be needed in order to observe the correct scaling of the TNTI thickness (Silva *et al.* 2018), and this Reynolds number threshold is far from being attained for JET_{106}.

Appendix E. Conditional enstrophy profiles for the IB and the envelope of the IB

The great majority of works devoted to the analysis of TNTIs use conditional statistics based on the envelope of the IB instead of the IB, and it may be useful to show what

https://doi.org/10.1017/jfm.2021.168 Published online by Cambridge University Press

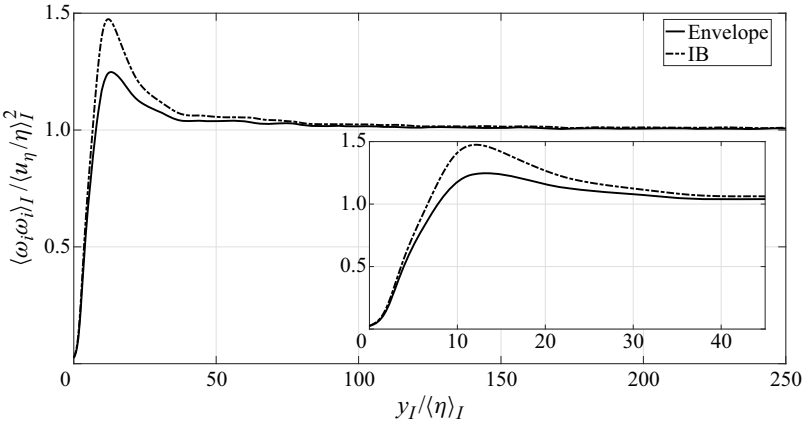

Figure 23. Comparison between the conditional mean enstrophy profiles $\langle\omega_i\omega_i\rangle_I$ using the IB and the interface enveloping the IB (described in § 2.2). The averaged profiles were obtained with all the simulations used in the present work (as shown in figure 5), where the profiles have been normalised with the local mean Kolmogorov velocity and length scale, computed at each coordinate y_I, $\langle\eta\rangle_I$ and $\langle u_\eta\rangle_I$, respectively. The inset shows the amplified region near the IB ($y_I = 0$).

happens to the normalised profiles of enstrophy when one uses the two metrics. For this purpose, figure 23 shows the normalised conditional mean enstrophy profiles obtained by using the envelope of the IB (as in all the figures of the present work) or the 'true' IB. Both profiles result from averaging the profiles of all the simulations used in the present work (excluding those that are only in the appendices).

The curves are virtually equal except between $5 \leq y_I/\langle\eta\rangle_I \leq 30$, the conditional enstrophy obtained with the IB exhibiting a stronger peak, roughly 15 % higher, although occurring at the same location. Thus, the difference between the two metrics is indeed small and is only felt in the magnitude of the peak of enstrophy.

References

Alvelius, K. 1999 Random forcing of three-dimensional homogeneous turbulence. *Phys. Fluids* **11** (7), 1880–1889.

Attili, A., Cristancho, J.C. & Bisetti, F. 2014 Statistics of the turbulent/non-turbulent interface in a spatially developing mixing layer. *J. Turbul.* **15**, 555–568.

Bisset, D.K., Hunt, J.C.R. & Rogers, M.M. 2002 The turbulent/non-turbulent interface bounding a far wake. *J. Fluid Mech.* **451**, 383–410.

Blackburn, H., Mansour, N. & Cantwell, B. 1996 Topology of fine-scale motions in turbulent channel flow. *J. Fluid Mech.* **310**, 269–292.

Borrell, G. & Jiménez, J. 2016 Properties of the turbulent/non-turbulent interface in boundary layers. *J. Fluid Mech.* **801**, 554–596.

Breda, M. & Buxton, O.R.H. 2019 Behaviour of small-scale turbulence in the turbulent/non-turbulent interface region of developing turbulent jets. *J. Fluid Mech.* **879**, 187–216.

Cantwell, B. 1993 On the behavior of velocity gradient tensor invariants in direct numerical simulations of turbulence. *Phys. Fluids* **5** (8), 2008–2013.

Canuto, C., Hussaini, M.Y., Quarteroni, A. & Zang, T.A. 1987 *Spectral Methods in Fluid Dynamics*. Springer-Verlag.

Chauhan, K., Philip, J. & Marusic, I. 2014*a* Scaling of the turbulent/non-turbulent interface in boundary layers. *J. Fluid Mech.* **751**, 1–31.

Chauhan, K., Philip, J., de Silva, C.M., Hutchins, N. & Marusic, I. 2014*b* The turbulent/non-turbulent interface and entrainment in a boundary layer. *J. Fluid Mech.* **742**, 119–151.

Chong, M.S., Soria, J., Perry, A.E., Chacin, J., Cantwell, B.J. & Na, Y. 1998 Turbulence structures of wall-bounded shear flows found using DNS data. *J. Fluid Mech.* **357**, 225–247.

https://doi.org/10.1017/jfm.2021.168 Published online by Cambridge University Press

CIMARELLI, A., COCCONI, G., FROHNAPFEL, B. & ANGELIS, E.D. 2015 Spectral enstrophy budget in a shear-less flow with turbulent/non-turbulent interface. *Phys. Fluids* **27**, 125106.

CORRSIN, S. & KISTLER, A.L. 1955 Free-stream boundaries of turbulent flows. *Tech. Rep.* TN-1244. Neighborhood Assistance Corporation of America. pp. 1033–1064.

DAVIDSON, P.A. 2004 *Turbulence, An Introduction for Scientists and Engineers*. Oxford University Press.

DONZIS, D.A. & SREENIVASAN, K.R. 2010 The bottleneck effect and the Kolmogorov constant in isotropic turbulence. *J. Fluid Mech.* **657**, 171–188.

ELSINGA, G. & MARUSIC, I. 2010 Universal aspects of small-scale motions in turbulence. *J. Fluid Mech.* **662**, 514–539.

GEORGE, W.K. 1989 The self-preservation of turbulent flows and its relation to initial conditions and coherent structures. In *Advances in Turbulence* (ed. R. Arndt & W.K. George), pp. 39–73. Hemisphere.

GOMES-FERNANDES, R., GANAPATHISUBRAMANI, B. & VASSILICOS, J.C. 2014 Evolution of the velocity-gradient tensor in a spatially developing turbulent flow. *J. Fluid Mech.* **756**, 252–292.

GUIMARÃES, M.C., PIMENTEL, N., PINHO, F.T. & DA SILVA, C.B. 2020 Direct numerical simulations of turbulent viscoelastic jets. *J. Fluid Mech.* **899**, 11–37.

HOLZNER, M., LIBERZON, A., LUTHI, B., NIKITIN, N., KINZELBACH, W. & TSINOBER, A. 2008 A lagrangian investigation of the small-scale features of turbulent entrainment through particle tracking and direct numerical simulation. *J. Fluid Mech.* **598**, 465–475.

HOLZNER, M., LIBERZON, A., NIKITIN, N., KINZELBACH, W. & TSINOBER, A. 2007 Small-scale aspects of flows in proximity of the turbulent/nonturbulent interface. *Phys. Fluids* **19**, 071702.

HOLZNER, M. & LUTHI, B. 2011 Laminar superlayer at the turbulence boundary. *Phys. Rev. Lett.* **106**, 134503.

HOLZNER, M., LUTHI, B., TSINOBER, A. & KINZELBACH, W. 2009 Acceleration, pressure and related quantities in the proximity of the turbulent/non-turbulent interface. *J. Fluid Mech.* **639**, 153–165.

ISHIHARA, T., KANEDA, Y., YOKOKAWA, M., ITAKURA, K. & UNO, A. 2007 Small-scale statistics in high-resolution direct numerical simulation of turbulence: Reynolds number dependence of one-point velocity gradient statistics. *J. Fluid Mech.* **592**, 335–366.

ISHIHARA, T., OGASAWARA, H. & HUNT, J.C.R. 2015 Analysis of conditional statistics obtained near the turbulent/non-turbulent interface of turbulent boundary layers. *J. Fluids Struct.* **53**, 50–57.

JAHANBAKHSHI, R. & MADNIA, C.K. 2016 Entrainment in a compressible turbulent shear layer. *J. Fluid Mech.* **797**, 564–603.

JAHANBAKHSHI, R. & MADNIA, C.K. 2018 The effect of heat release on the entrainment in a turbulent mixing layer. *J. Fluid Mech.* **844**, 92–126.

LESIEUR, M., OSSIA, S. & MÉTAIS, O. 1999 Infrared pressure spectra in 3D and 2D isotropic incompressible turbulence. *Phys. Fluids* **11**, 1535–1543.

MISTRY, D., PHILIP, J. & DAWSON, J.R. 2019 Kinematics of local entrainment and detrainment in a turbulent jet. *J. Fluid Mech.* **871**, 896–924.

MOSER, R.D., ROGERS, M.M. & EWING, D.W. 1998 Self-similarity of time-evolving plane wakes. *J. Fluid Mech.* **367**, 255–289.

OOI, A., MARTIN, J., SORIA, J. & CHONG, M. 1999 A study of the evolution and characteristics of the invariants of the velocity-gradient tensor in isotropic turbulence. *J. Fluid Mech.* **381**, 141–174.

PEROT, B. & MOIN, P. 1995 Shear-free turbulent boundary layers. Part 1. Physical insights into near-wall turbulence. *J. Fluid Mech.* **295**, 199–227.

POPE, S.B. 1985 PDF methods for turbulent reactive flows. *Prog. Energy Combust. Sci.* **11**, 119–192.

POPE, S.B. 2000 *Turbulent Flows*. Cambridge University Press.

RAMAPRIAN, B.R., KALALE, K.P.L., JOVIC, S. & KAUSHIK, S. 1984 Study of large-scale mixing in developing wakes behind streamlined bodies. *Tech. Rep.* CR-173478. National Aeronautics and Space Administration.

VAN REEUWIJK, M. & HOLZNER, M. 2014 The turbulence boundary of a temporal jet. *J. Fluid Mech.* **739**, 254–275.

ROGERS, M.M. & MOSER, R.D. 1994 Direct simulation of a self-similar turbulent mixing layer. *Phys. Fluids* **6** (2), 903–923.

DA SILVA, C.B., HUNT, J.C.R., EAMES, I. & WESTERWEEL, J. 2014 Interfacial layers between regions of different turbulent intensity. *Annu. Rev. Fluid Mech.* **46**, 567–590.

DA SILVA, C.B., LOPES, D.C. & RAMAN, V. 2015 The effect of subgrid-scale models on the entrainment of a passive scalar in a turbulent planar jet. *J. Turbul.* **16** (4), 342–366.

DA SILVA, C.B. & PEREIRA, J.C.F. 2008 Invariants of the velocity-gradient, rate-of-strain, and rate-of-rotation tensors across the turbulent/nonturbulent interface in jets. *Phys. Fluids* **20**, 055101.

DA SILVA, C.B. & PEREIRA, J.C.F. 2009 Erratum: 'invariants of the velocity-gradient, rate-of-strain, and rate-of-rotation tensors across the turbulent/nonturbulent interface in jets' [Phys. Fluids, 20, 055101, 2008]. *Phys. Fluids* **21**, 019902.

https://doi.org/10.1017/jfm.2021.168 Published online by Cambridge University Press

DA SILVA, C.B., DOS REIS, R.J.N. & PEREIRA, J.C.F. 2011 The intense vorticity structures near the turbulent/non-turbulent interface a jet. *J. Fluid Mech.* **685**, 165–190.

SILVA, T.S. & DA SILVA, C.B. 2017 The behaviour of the scalar gradient across the turbulent/non-turbulent interface in jets. *Phys. Fluids* **29**, 085106.

DA SILVA, C.B. & TAVEIRA, R.R. 2010 The thickness of the turbulent/nonturbulent interface is equal to the radius of the large vorticity structures near the edge of the shear layer. *Phys. Fluids* **22**, 121702.

SILVA, T.S., ZECCHETTO, M. & DA SILVA, C.B. 2018 The scaling of the turbulent/non-turbulent interface at high reynolds numbers. *J. Fluid Mech.* **843**, 156–179.

SORIA, J., SONDERGAARD, R., CANTWELL, B., CHONG, M. & PERRY, A. 1994 A study of the fine-scale motions of incompressible time-developing mixing layers. *Phys. Fluids* **6** (2), 871–884.

STANLEY, S., SARKAR, S. & MELLADO, J.P. 2002 A study of the flowfield evolution and mixing in a planar turbulent jet using direct numerical simulation. *J. Fluid Mech.* **450**, 377–407.

TAVEIRA, R.R., DIOGO, J.S., LOPES, D.C. & DA SILVA, C.B. 2013 Lagrangian statistics across the turbulent-nonturbulent interface in a turbulent plane jet. *Phys. Rev.* E **88**, 043001.

TAVEIRA, R.R. & DA SILVA, C.B. 2013 Kinetic energy budgets near the turbulent/nonturbulent interface in jets. *Phys. Fluids* **25**, 015114.

TAVEIRA, R.R. & DA SILVA, C.B. 2014 Characteristics of the viscous superlayer in free shear turbulence and in planar turbulent jets. *Phys. Fluids* **26**, 021702.

TEIXEIRA, M.A.C. & DA SILVA, C.B. 2012 Turbulence dynamics near a turbulent/non-turbulent interface. *J. Fluid Mech.* **695**, 257–287.

TOWNSEND, A.A. 1976 *The Structure of Turbulent Shear Flow*. Cambridge University Press.

TSINOBER, A. 2019 *The Essence of Turbulence as a Physical Phenomenon*. Kluwer Academic Publishers.

TSINOBER, A., ORTENBERG, M. & SHTILMAN, L. 1999 On depression of nonlinearity in turbulence. *Phys. Fluids* **11** (8), 2291–2297.

VAGHEFI, N.S. & MADNIA, C.K. 2015 Local flow topology and velocity gradient invariants in compressible turbulent mixing layer. *J. Fluid Mech.* **774**, 67–94.

WATANABE, T., JAULINO, R., TAVEIRA, R., DA SILVA, C.B., NAGATA, K. & SAKAI, Y. 2017*a* Role of an isolated eddy near the turbulent/non-turbulent interface layer. *Phys. Rev. Fluids* **2**, 094607.

WATANABE, T., NAGATA, K. & DA SILVA, C.B. 2017*b* Vorticity evolution near the turbulent/non-turbulent interfaces in free-shear flows. In *Vortex Structures in Fluid Dynamic Problems* (ed. Dr. H. Perez-De-Tejada), pp. 1–18. InTech.

WATANABE, T., RILEY, J.J., DE BRUYN KOPS, S.M., DIAMESSIS, P.J. & ZHOU, Q. 2016*a* Turbulent/non-turbulent interfaces in wakes in stably stratified fluids. *J. Fluid Mech.* **797**, 1–11.

WATANABE, T., RILEY, J.J. & NAGATA, K. 2017*c* Turbulent entrainment across turbulent-nonturbulent interfaces in stably stratified mixing layers. *Phys. Rev. Fluids* **2** (10), 104803–104823.

WATANABE, T., SAKAI, Y., NAGATA, K., ITO, Y. & HAYASE, T. 2014 Enstrophy and passive scalar transport near the turbulent/non-turbulent interface in a turbulent planar jet flow. *Phys. Fluids* **26**, 105103.

WATANABE, T., DA SILVA, C.B. & NAGATA, K. 2019 Non-dimensional energy dissipation rate near the turbulent/non-turbulent interfacial layer in free shear flows and shear free turbulence. *J. Fluid Mech.* **875**, 321–344.

WATANABE, T., DA SILVA, C.B., SAKAI, Y., NAGATA, K. & HAYASE, T. 2016*b* Lagrangian properties of the entrainment across turbulent/non-turbulent interface layers. *Phys. Fluids* **28**, 031701.

WATANABE, T., ZHANG, X. & NAGATA, K. 2018 Turbulent/non-turbulent interfaces detected in DNS of incompressible turbulent boundary layers. *Phys. Fluids* **30** (3), 035102.

WESTERWEEL, J., FUKUSHIMA, C., PEDERSEN, J.M. & HUNT, J.C.R. 2005 Mechanics of the turbulent-nonturbulent interface of a jet. *Phys. Rev. Lett.* **95**, 174501.

WESTERWEEL, J., FUKUSHIMA, C., PEDERSEN, J.M. & HUNT, J.C.R. 2009 Momentum and scalar transport at the turbulent/non-turbulent interface of a jet. *J. Fluid Mech.* **631**, 199–230.

WESTERWEEL, J., HOFMANN, T., FUKUSHIMA, C. & HUNT, J.C.R. 2002 The turbulent/non-turbulent interface at the outer boundary of a self-similar turbulent jet. *Exp. Fluids* **33**, 873.

WEYGANDT, J.H. & MEHTA, R.D. 1995 Three-dimensional structure of straight and curved plane wakes. *J. Fluid Mech.* **282**, 279–311.

WILLIAMSON, J.H. 1980 Low-storage Runge–Kutta schemes. *J. Comput. Phys.* **35**, 48–56.

WYGNANSKI, I., CHAMPAGNE, F. & MARASLI, B. 1986 On the large-scale structures in two-dimensional, small-deficit, turbulent wakes. *J. Fluid Mech.* **168**, 31–71.

ZHOU, Y. & ANTONIA, R.A. 1995 Memory effects in a turbulent plane wake. *Exp. Fluids* **19** (2), 112–120.

https://doi.org/10.1017/jfm.2021.168 Published online by Cambridge University Press